

# Numerical Modeling of the Effect of Moisture Migration and Evaporation on the Temperature of Internal Wall Surfaces in Tunnels

by

Mansoureh MOUCHAN

THESIS PRESENTED TO ÉCOLE DE TECHNOLOGIE SUPÉRIEURE  
IN PARTIAL FULFILLEMENT FOR A MASTER'S DEGREE  
WITH THESIS IN CONSTRUCTION ENGINEERING  
M.A.Sc.

MONTREAL, MARCH 22, 2023

ÉCOLE DE TECHNOLOGIE SUPÉRIEURE  
UNIVERSITÉ DU QUÉBEC



Mansoureh Mouchan, 2023



This Creative Commons licence allows readers to download this work and share it with others as long as the author is credited. The content of this work can't be modified in any way or used commercially.

**BOARD OF EXAMINERS**

THIS THESIS HAS BEEN EVALUATED

BY THE FOLLOWING BOARD OF EXAMINERS

Mr. François Duhaime, Thesis Supervisor  
Department of Construction Engineering, École de technologie supérieure

Mr. Wahid Maref, President of the Board of Examiners  
Department of Construction Engineering, École de technologie supérieure

Mr. Jean-Sébastien Dubé, Member of the Jury  
Department of Construction Engineering, École de technologie supérieure

THIS THESIS WAS PRESENTED AND DEFENDED

IN THE PRESENCE OF A BOARD OF EXAMINERS AND PUBLIC

MARCH 15, 2023

AT ÉCOLE DE TECHNOLOGIE SUPÉRIEURE



## **ACKNOWLEDGMENT**

It is my pleasure to express my gratitude to my supervisor, professor Francois Duhaime, for his support during my master's program. As a student, I was very fortunate to have his wise advice, support, and encouragement during my studies.

My sincere thanks go out to the board of examiners for taking the time to review my master's thesis.

A special thanks goes out to my family for the endless support, inspiration, and encouragement they have provided for me during my studies.



# **Modélisation numérique de l'effet de la migration et de l'évaporation de l'humidité sur la température des parois internes des tunnels**

Mansoureh MOUCHAN

## **RÉSUMÉ**

Les tunnels sont vulnérables aux infiltrations d'eau. L'infiltration d'eau peut causer des dommages importants à la structure des tunnels. Les revêtements des tunnels, les structures en béton et les équipements peuvent être affectés au fil du temps par l'infiltration d'eau. Les fuites d'eau sont le plus souvent causées par des joints de construction et de dilatation (Ji et al., 2012). Localiser et caractériser les infiltrations d'eau associées aux joints est une préoccupation majeure pour la sécurité et l'entretien des tunnels.

La présence d'eau dans le béton influence ses propriétés d'échange thermique et sa température. L'influence des échanges thermiques peut être détectée par thermographie infrarouge, une méthode d'imagerie non destructive qui permet de déterminer à distance la température d'une surface. L'imagerie thermique permet de localiser et de caractériser les infiltrations d'eau dans différentes structures telles que les tunnels. À ce jour, aucune méthode quantitative n'a été développée pour mesurer l'infiltration dans les tunnels grâce à l'utilisation de la thermographie infrarouge (M'nasri, 2020).

Dans cette étude, L'effet de la variation de l'humidité relative, de la température de l'air, de la température de l'eau, du coefficient de convection et de la perméabilité du matériau sur la température du béton a été étudié à l'aide d'un modèle numérique. Une étude paramétrique a été menée avec le modèle numérique d'un joint de dilatation. Le modèle numérique a été développé sur la base du modèle physique qui a été construit par M'nasri (2020).

Le modèle numérique a été validé avec les températures mesurées avec le modèle physique. La bonne corrélation obtenue avec les cas de test respectifs montre que le modèle peut être appliqué pour évaluer le comportement thermique des parois du tunnel.

Les résultats montrent l'importance de l'humidité relative et des conditions environnementales sur la température de la surface de la paroi à l'intérieur du tunnel. Les joints dans un environnement à humidité relative plus élevée auront une température plus élevée en raison du taux d'évaporation plus lent. L'anomalie de température d'un joint qui fuit varie avec la différence entre les températures de l'eau et de l'air. Pour des valeurs de perméabilité des joints comprises entre  $1 \times 10^{-17} \text{ m}^2$  et  $1 \times 10^{-15} \text{ m}^2$ , les conditions environnementales contrôlent l'anomalie de température. Pour une perméabilité supérieure à  $1 \times 10^{-13} \text{ m}^2$ , l'anomalie de température est contrôlée par la température de la nappe phréatique. La diminution de température au niveau du joint augmente avec une augmentation du coefficient de convection. Avec une augmentation de la différence de température entre l'air et l'eau, l'anomalie de température associée à un joint qui fuit augmente également. Les résultats montrent qu'une augmentation de la perméabilité entraîne une chute de température plus élevée de la surface du

## VIII

joint. Pour une humidité relative plus élevée, il est difficile de détecter la variation de température associée aux perméabilités proches.

**Mots-clés:** infiltration d'eau, joints de dilatation, modèle numérique, température du béton, thermographie infrarouge

# **Numerical modeling of the effect of moisture migration and evaporation on the temperature of internal wall surfaces in tunnels**

Mansoureh MOUCHAN

## **ABSTRACT**

Tunnels are vulnerable to water infiltration. Water infiltration can cause significant damage to tunnel structure. Tunnel linings, concrete structures, and equipment can be adversely affected over time by water infiltration. Water leaks are most commonly caused by construction and expansion joints (Ji et al., 2012). Locating and characterizing the water infiltration associated with joints is a major concern for the safety and maintenance of tunnels.

The presence of water in concrete influences its heat exchange properties and temperature. The influence of heat exchanges can be detected by infrared thermography, a non-destructive imaging method that allows the temperature of a surface to be determined from a distance. Thermal imaging can locate and characterize water infiltration in different structures such as tunnels. As of yet, no quantitative method has been developed to measure infiltration in tunnels through the use of infrared thermography (M'nasri, 2020).

In this study, the effect of variation in relative humidity, air temperature, water temperature, convection coefficient, and material permeability on concrete temperature was investigated using a numerical model. A parametric study was conducted with the numerical model of an expansion joint. The numerical model was developed based on the physical model that was constructed by M'nasri (2020).

The numerical model was validated with the temperatures measured with the physical model. The good correlation obtained with the respective test cases shows that the model can be applied to evaluate the thermal behavior of the tunnel walls.

The results show the importance of relative humidity and environmental conditions on the temperature of the wall surface inside the tunnel. Joints in a higher relative humidity environment will have a higher temperature because of the slower rate of evaporation. The temperature anomaly of a leaking joint varies with the difference between the water and air temperatures. For joint permeability values between  $1 \times 10^{-17} \text{ m}^2$  and  $1 \times 10^{-15} \text{ m}^2$ , the environmental conditions control the temperature anomaly. For permeability greater than  $1 \times 10^{-13} \text{ m}^2$ , the temperature anomaly is controlled by groundwater temperature. The temperature decrease at the joint with an increase in convection coefficient. With an increase of the temperature difference between air and water, the temperature anomaly associated with a leaking joint also increases. The results show an increase in permeability causes the joint surface to experience a higher temperature drop. For higher relative humidity, it is difficult to detect the temperature variation associated to close permeabilities.

**Keywords:** water infiltration, expansion joints, numerical model, concrete temperature, infrared thermography

## TABLE OF CONTENTS

	Page
INTRODUCTION.....	1
CHAPTER 1 LITERATURE REVIEW .....	3
1.1 Tunnel damages .....	3
1.2 Water infiltration.....	3
1.2.1 Main cause of water infiltration.....	4
1.2.2 Methods for detecting water infiltration .....	6
1.3 Infrared thermography .....	6
1.3.1 Infrared thermography basic concepts and data.....	7
1.3.2 Application of infrared thermography for ground water .....	9
1.3.3 Advantages and limitations of infrared thermography .....	11
1.4 Numerical modelling .....	13
1.4.1 Heat and moisture transfer .....	14
1.4.2 Governing equations .....	14
1.4.3 Water conservation equation in porous media.....	14
1.4.4 Heat conservation equation in porous media .....	16
CHAPTER 2 METHODOLOGY .....	19
2.1 Physical model.....	19
2.1.1 Description and construction of the physical model.....	19
2.1.2 Test procedure.....	22
2.2 Numerical model.....	23
2.2.1 Geometry and mesh .....	23
2.2.2 Governing equations and boundary conditions.....	24
2.2.3 Parametric study.....	29
CHAPTER 3 RESULTS AND DISCUSSION.....	31
3.1 Model validation and calibration .....	31
3.2 Parametric study.....	35
3.2.1 Relative humidity .....	36
3.2.2 Air and water temperatures .....	38
3.2.3 Convection coefficient .....	42
3.2.4 Joint permeability.....	43
3.2.5 Temperature anomaly graphs.....	46
CONCLUSION.....	51
RECOMMENDATIONS.....	53
REFERENCES.....	55



## LIST OF FIGURES

	Page
Figure 1.1	Expansion joint and ice in tunnel.....5
Figure 1.2	Range of IR spectrum .....7
Figure 1.3	Measurement of vertical temperature gradient from the artificial .....10
Figure 2.1	Diagram of the physical model of the expansion joints.....20
Figure 2.2	A surface of physical model of.....21
Figure 2.3	Arrangement of thermocouples and data acquisition.....21
Figure 2.4	Water circulation for two phase of tests .....22
Figure 2.5	The model domain in this study.....24
Figure 2.6	Flowchart for the flux boundary condition at the concrete surface. ....27
Figure 2.7	Summary of boundary conditions on the model.....28
Figure 3.1	Three series of infrared thermographs. ....31
Figure 3.2	Temperature calibration for the numerical model .....33
Figure 3.3	2D section of the model with temperature colour grid. ....34
Figure 3.4	Comparison between the surface temperature measured.....35
Figure 3.5	Influence of relative humidity on temperature .....37
Figure 3.6	Influence of relative humidity on the heat flux component.....37
Figure 3.7	Influence of air temperature on the concrete surface temperature.....38
Figure 3.8	Influence of water temperature variation on the temperature on.....39
Figure 3.9	Heat flux components for $T_{air} = 20.5\text{ }^{\circ}\text{C}$ and $T_{water} = 13\text{ }^{\circ}\text{C}$ .....40
Figure 3.10	Heat flux components for $T_{air} = 25\text{ }^{\circ}\text{C}$ and $T_{water} = 5\text{ }^{\circ}\text{C}$ .....41
Figure 3.11	Heat flux components for $T_{air} = 5\text{ }^{\circ}\text{C}$ and $T_{water} = 15\text{ }^{\circ}\text{C}$ .....42
Figure 3.12	Influence of hydraulic conductivity on the temperature.....43

Figure 3.13	Influence of joint permeability on the temperature.....	44
Figure 3.14	Comparison of temperature on the concrete .....	44
Figure 3.15	Influence of relative humidity and permeability.....	45
Figure 3.16	Location of temperature values for temperature anomaly graphs .....	47
Figure 3.17	Points on the temperature curve.....	47
Figure 3.18	Influence of relative humidity on temperature anomalies .....	48
Figure 3.19	Influence of coefficient of convection .....	50
Figure 3.20	Influence of water and air temperature variation.....	50

## LIST OF SYMBOLS AND UNITS OF MEASUREMENT

$^{\circ}\text{C}$	Centigrade
$c_l$	Heat capacity of water ( $\text{J}\cdot\text{kg}^{-1}\cdot\text{K}^{-1}$ )
$c_p$	Thermal mass capacity ( $\text{J}\cdot\text{kg}^{-1}\cdot\text{K}^{-1}$ )
$c$	Speed of light
$g$	Acceleration of gravity ( $\text{m}\cdot\text{s}^{-2}$ )
$h$	Planck's constant
$h_c$	Convection coefficient $\text{W}/(\text{m}^2\cdot\text{K})$ .
$h_r$	Relative humidity
$J_l$	Liquid flux ( $\text{kg}\cdot\text{m}^{-2}\cdot\text{s}^{-1}$ )
$J_v$	Evaporation in boundary condition ( $\text{kg}\cdot\text{m}^{-2}\cdot\text{s}^{-1}$ )
$J_v$	Vapour flux ( $\text{kg}\cdot\text{m}^{-2}\cdot\text{s}^{-1}$ ) inside domain
K	Kelvin
$K_l$	Hydraulic conductivity ( $\text{m}\cdot\text{s}^{-1}$ )
$k_l$	Concrete intrinsic permeability ( $\text{m}^2$ )
$K_T$	Effective thermal conductivity ( $\text{W}\cdot\text{m}^{-1}\cdot\text{K}^{-1}$ )
$k$	Boltzmann's constant
m	Meter
$N_{\lambda}$	Infrared radiation by a real object
$N_{\lambda,b}$	Theoretical blackbody radiation
$P_l$	Pore water pressure ( $\text{Nm}^{-2}$ )
$Q_T$	Local heat source ( $\text{J}\cdot\text{s}^{-1}\cdot\text{m}^{-3}$ ).
$R_v$	Gas constant for water in vapor condition in $\text{J}/\text{kg}$
$T$	Temperature
$T_{air}$	Air temperature
$T_{concrete}$	Concrete temperature
$T_{water}$	Water temperature
$w$	Water content ( $w$ )

$\varepsilon$	Emissivity
$\partial h / \partial y$	Hydraulic gradient
$\Delta h_v$	Latent heat of water evaporation (J / kg)
$\Theta_p$	Porosity of solid in porous media
$\lambda$	Wavelength of the radiation emitted by the black body
$\mu_l$	Water dynamic viscosity (Pa·s)
$\rho_a$	Density of air ( $\text{kg}\cdot\text{m}^{-3}$ )
$\rho_l$	Water density ( $\text{kg}\cdot\text{m}^{-3}$ )
$\Theta_p$	Porosity of solid in porous media
$\lambda$	wavelength of the radiation emitted by the black body
$\mu_l$	Water dynamic viscosity (Pa·s)
$\rho_a$	Density of air ( $\text{kg}\cdot\text{m}^{-3}$ )

## INTRODUCTION

Water infiltration is an old and common problem in tunnel construction and maintenance (Li et al., 2009). Construction and expansion joints are considered to be the main source of water infiltration in tunnels (Ji et al., 2012). Tunnel linings are susceptible to progressive failure due to joint damage (Gong et al., 2018). For tunnels in colder climates, during the winter, the existence of water might result to the formation of ice, which eventually leads to the degradation of steel and structural concrete. Periodic inspections are vital to make sure that the structure is safe for user over the time (Wimsatt et al., 2013).

There are multiple methods to investigate water infiltration. Infrared thermography is one of the most popular and effective method to detect water infiltration (Kylili et al., 2014). Thermography can provide a fast evaluation of groundwater seepage zones. When water evaporates from a concrete surface, heat is required which results in a decrease in the concrete surface temperature (Barreira et al., 2015). Therefore, the state of leakage joints can be determined using infrared thermography. As a result, the defects can be ranked by the degree of flow and finally repairs can be prioritized based on surface anomalies.

Infrared thermography has a number of limitations, as do other approaches. The relationship between the temperature anomaly and the flow rate through a defective joint is complex. The temperature at the concrete surface depends on the flow rate, but also on the atmospheric conditions in the tunnel, the groundwater temperature, and material properties. Methods based on infrared thermography currently only provide qualitative information. There is currently no quantitative method to determine the flow rate associated with water infiltration in tunnels based on infrared thermography (Lu et al., 2019).

Physical and numerical modeling are two methods that can help to study the effect of water infiltration on the temperature of wall based on thermal images. A physical model of expansion joints was constructed at ÉTS by M'nasri (2020). The physical model was designed to investigate the effect of temperature change on the expansion joints with different permeability

inside the tunnel, and find the possible relationship between joint permeabilities, leakage rate and temperature anomalies observed by using thermographic image on concrete surface. One of the objectives of the physical model was to generate temperature data to calibrate a numerical model.

In this study a numerical model is developed according to M'nasri (2020) experimental model. To achieve the quantitative relationships between the main factors due to moisture transfer, parametric study is performed on the numerical modeling to study the link between variation of different factors and temperature anomaly on the joint and on the surface of concrete. There is also an objective to represent a connection between the variation of the temperature of the concrete surface, the permeability of joints utilizing parametric studies.

This thesis contains 3 chapters. Chapter 1 presents a literature review on water infiltration in tunnels, infrared thermography, and the governing equations for heat transfer and seepage in porous media. A description of the methodology used in this study is provided in Chapter 2, including the construction of the physical model and the development of the finite element model. Chapter 3 presents a validation of the numerical model with the physical model results and a parametric study.

## CHAPTER 1

### LITERATURE REVIEW

#### 1.1 Tunnel damages

Highway tunnels throughout the world are aging and need to be repaired, often while they are being used by people. Multiple problems are associated with the aging of tunnels including crack formation, water infiltration, frost damage, icing problems, corrosion of reinforcement, decrease in strength of concrete and problems associated to drainage. Specific damage types usually do not happen alone. For example, in cold regions and old tunnels, lining cracks might lead to water leakage. Water leakage can then lead to frost damage (Yuan et al., 2011). Aging usually leads to damages to the lining of tunnels (Toshihiro et al., 2003).

Some internal and external factors can contribute to the deterioration of tunnels. External factors include frost damage, the effect of smoke, and salt damage (Toshihiro et al., 2003). Internal factors include problematic materials, insufficient cement in concrete, improper joint filling and finally some internal damage could be related to alkali-aggregate mechanism (Toshihiro et al., 2003).

#### 1.2 Water infiltration

Damages due to water infiltration are often considered to be more important than the other damages (Yuan et al., 2011; Toshihiro et al., 2003). For tunnels located in cold regions, the data show that the lining cracks and water infiltration are the most significant type of damage (Yuan et al., 2011). The migration of moisture also affects the temperature of structures and the quality of internal environments (Dong et al., 2020).

Water leakage might lead to serious hazard in tunnels. Some of the worst disasters that have happened in tunnels have been caused by high volumes of water infiltration from fractured rock (Li et al., 2009). One of those cases concerns the construction of the Pinglin tunnels of

the Taipei-Ilan expressway. The discharge of water infiltration was more than 750 l/s (Tseng et al., 2001). It caused the closure of the tunnel heading and damaged to the tunnel boring machine (TBM)(Li et al., 2009).

Tunnel boring machine (TBM) is a method of drilling tunnels. It is particularly suitable for urban tunneling where the work is typically carried out close to the surface of the ground (Font Capó, 2012). During the construction of tunnels using TBMs, water infiltration might poses serious problems. An influx of groundwater can adversely affect the performance of TBMs and cause damage to concrete tunnel linings (Solecki et al., 2022).

### **1.2.1 Main cause of water infiltration**

To find the best solution for water leakage problems, it is necessary to understand the main causes of water infiltration. There are three types of water infiltration: water infiltration from construction and expansion joints, water infiltration from lining cracks, and water infiltration from voids behind the lining (Shijie et al., 2020).

Water infiltration from construction joint is one of the most common forms of water infiltration. During construction , the concrete material cannot be placed in a continuous manner practically. Therefore, it is necessary to ensure that concrete is placed in sequence without damaging the structure (Nawy, 2008). Improper concrete compaction around the water stop strip may be led to water infiltration through the joints (Locatelli et al., 2001). In construction joint water easily find its way through various joints. These joints can connect to a groundwater source and finally discharge a high volume of water inside the tunnel.

Lining cracks usually form after the construction phase. Lining cracks are mainly due to the pressure on the tunnel lining. The temperature variation and settlements of the tunnel can also lead to the formation of cracks (Shijie et al., 2020). Water travel through these cracks and seep on the surface. This seepage will eventually erode the tunnel internal structure and might cause erosion and corrosion of the metal components in the tunnel over time. The deterioration of

the tunnel structure is increased by ions present in the water seeping through the structures like chloride ions (Morin-Morissette, 2016).

The voids located behind the lining are formed as a result of construction of the tunnel. All excavation procedures make the cracks and cavity wider (Shijie et al., 2020). The effect of freeze-thaw cycles can accelerate the formation of cracks and voids. The water freezes due to cold weather. As the volume expands, a large force is applied to a structure. It causes an increase in the hydraulic pressure in the concrete. Finally, it will lead to tunnel degradation (Mainali et al., 2015). Figure 1.1 shows an example of this phenomenon.



Figure 1.1 Expansion joint and ice in the tunnel  
Taken from CETU (2015)

Infiltration can also lead to erosion of granular rocks and soils outside tunnels. This erosion is able to create voids inside tunnels. Particularly, such damage makes the concrete wavy and soft and finally will make a water path (Shijie et al., 2020).

Water infiltration due to fractured lining: this problem is influenced by many factors, which are usually occurring during the working time of tunnels. For example, loose areas of lining, poor concrete compaction are the reason of breaking lining (Shijie et al., 2020).

To control water infiltration through the concrete structure of tunnels, a strong drainage system is necessary. In most cases, designers fail to include a channel for water seepage in joints during

construction. A proper drainage system helps the water travel through the drainage path and to be discharged safely (Ji et al, 2012).

### **1.2.2 Methods for detecting water infiltration**

Tunnel inspection is a difficult task because tunnels are aggressive environments and because it is often required to keep the tunnels open during inspection or to minimise the closure duration. For these reasons, non-destructive methods are often used. Non-destructive methods provide automated, quantitative, faster results and have more coverage than conventional methods (Wimsatt et al., 2013). Conventional methods include methods which demands more personnel to periodic direct observation and sometimes need more drilling on the surface of concrete. Non-destructive methods for water infiltration include air-coupled Ground Penetrating Radar (GPR), ground-coupled GPR, infrared thermography, and the SPACETEC scanner which use the most recent scanning technique (Wimsatt et al., 2013). Among those methods, infrared thermography is considered one of the most popular and effective non-destructive method (Kylili et al, 2014).

### **1.3 Infrared thermography**

Infrared thermography is considered a relatively new science in which the temperature information of a special surface record by a camera and then analysed for related interpretation (Williams et al., 2014). Infrared thermography is considering as a non-invasive imaging technique. It is an efficient method for periodic and rapid inspection of temperature-related features including water infiltration, heat loss, and lost or damaged thermal insulation in walls and ceilings (Lerma et al., 2011). This method provides a visual representation of heat-related issues.

### 1.3.1 Infrared thermography basic concepts and data

Infrared energy is dependent on absolute surface temperature. This energy radiates from every surface and gives us some indication of temperatures. Temperature distribution of a surface of an object can be seen by using infrared thermography.

Figure 1.2 shows the range of the infrared (IR) spectrum used for thermography. The part of the electromagnetic spectrum associated with thermal radiation begins near the UV band and continues throughout the visible and infrared wavebands. Infrared cameras use the three ranges of the IR spectrum which are presented in Figure 1.2. They include the long-wave region (LW) from 7 to 14  $\mu\text{m}$ , the medium wave region (MW) from 3 to 5  $\mu\text{m}$ , and the shortwave (SW) domain which start from  $\mu\text{m}$  0.9 and continues till to 1.7  $\mu\text{m}$  (Vollmer et al., 2010). Long-wavelength cameras are frequently used in thermal surveys of buildings. Because of their higher sensitivity to low temperatures, they can distinguish small temperature changes and be less affected by the reflections created by solar radiation (Lerma et al., 2011).

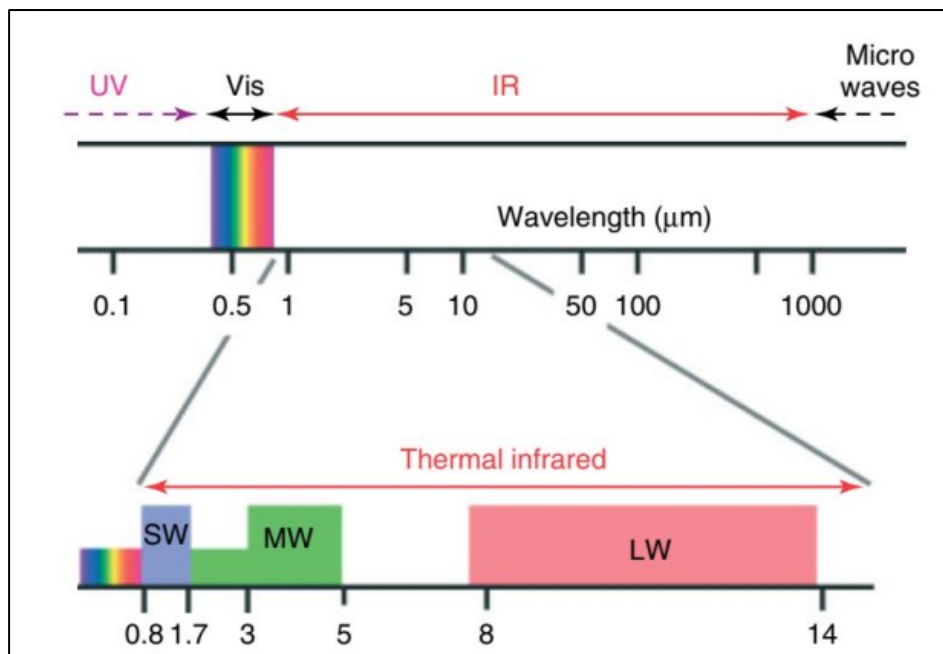


Figure 1.2 Range of IR spectrum  
Taken from Vollmer (2010)

It is not possible to detect the infrared energy by naked eyes. Infrared camera are devices that can image the infrared energy with a multicolored image. Data are gathered in the form of discrete quantitative measurement like video or image (Andrews et al., 2011). Thermal maps are also called IR temperature images or thermograms (Meola & Carlomagno, 2004). Thermograms present the temperature distribution on the surface of a specific object.

Planck's law is the basis of infrared thermography. It relates the infrared radiation of an idealized black body  $N_{\lambda,b}$  to its temperature ( $T$ ) in K as it can be seen in equation 1.1 (Maldague, 1993).

$$N_{\lambda,b} = \frac{2hc^2}{\lambda^5} \frac{1}{\exp\left(\frac{hc}{\lambda kT} - 1\right)} \quad (1.1)$$

$$N_{\lambda} = \varepsilon N_{\lambda,b}(\lambda, T) \quad (1.2)$$

where  $h$  describe Planck's constant,  $c$  describe the speed of light,  $k$  is Boltzmann's constant,  $T$  is the black body's temperature, and  $\lambda$  is the wavelength of the radiation emitted by the black body (Maldague, 1993). The proportion of energy emitted from a real object surface with respect to the energy that a blackbody can emit at the equal temperature defines the emissivity ( $\varepsilon$ ). Based on equation 1.2, the infrared radiation by a real object ( $N_{\lambda}$ ) depends on the object emissivity ( $\varepsilon$ ) and the theoretical blackbody radiation ( $N_{\lambda,b}$ ).

A black body symbolizes a physical body which can absorb all range of electromagnetic energy, irrespective of frequency or angle of incidence. When a real object absorbs energy electromagnetically, only a part of it will be radiated by its surface. This is making its emissivity lower than a black body. The emissivity ranges between 0 and 1. It depends on the material and the temperature of the emitted radiation, as well as the wavelength. When the emissivity of a body is below one, it reflects part of the ambient radiation. By assuming a value

for emissivity and also having knowledge of the surrounding environment's temperature, it is possible to estimate the temperature of a surface from the radiation it emits.

### **1.3.2 Application of infrared thermography for ground water**

Groundwater has constant temperature during the year. It is considered as a very important hydrologic tracer (Mundy et al. 2017). At a large scale, thermography can provide fast evaluations of groundwater seepage zones. Thermal signatures in groundwater can be used to find discrete discharge zones to surface water (Hare et al., 2015).

Thermal imagery can locate and characterize water infiltration in different structures such as tunnels. The existence of water through joints on the concrete influences heat exchanges in concrete. This heat flow makes a noticeable change on temperature pattern on the surface around the concrete. The heat flux controls by several factors, including the thermal conductivity of the porous area (Haack et al., 1995). Water in concrete affects both its thermal conductivity and its thermal capacity. During evaporation of water from a concrete surface, heat is required, which results in a decrease in the concrete temperature (Barreira et al., 2017). Due to the contrast between the temperature of groundwater, concrete, and air inside tunnels, it is possible to detect anomalies.

Temperature changes are lower in humid materials. The density, specific heat capacity, and thermal conductivity of a physical objects change when moisture is present (Lerma et al., 2011). Some physical properties should be considered in thermographic studies such as thermal properties including conductivity, specific heat, diffusivity and thermal conductivity and its volumetric heat capacity and spectral properties including transmissibility, adsorption, reflection, and transfer as well as other properties such as porosity, volumetric mass, and water content. Those properties have a great influence on behaviour of materials and how they react to temperature variation (Avdelidis & Moropoulou, 2004).

Infrared thermography can be applied to the evaluation of the hydraulic conductivity of fractured rock. Pappalardo (2018) showed that hydraulic conductivity can be correlated with the cooling rate of rock body, which is influenced by the spacing and aperture of joints in the rock mass (Pappalardo, 2018).

Mundy (2017) developed a conceptual model that shows the temperature variation in seepage on the rock surface, along with vertical distance from the fractures start point (vertical temperature gradient) is highly dependent to convection heat flow and water flow discharge. This study also demonstrates the flow of ground water can be detected from thermal images in the winter. During the summer, thermal images can aid to find distinction between low and high flow infiltration, by utilize a vertical temperature gradient from the source of water discharge to the vertical rock surface (Mundy et al., 2017). Based on the qualitative results of this study, Figure 1.3 (a) shows that the temperature gradient is lower for higher flows. As a result, less warming is experienced down the rock surface compared to flows at lower levels. In Figure 1.3 (b) the study illustrates how fractures and small complexities shifted and modified the flow of water on the rock surface. The inability to capture vertical temperature gradients accurately was hampered by these complexities and fractures (Mundy et al., 2017).

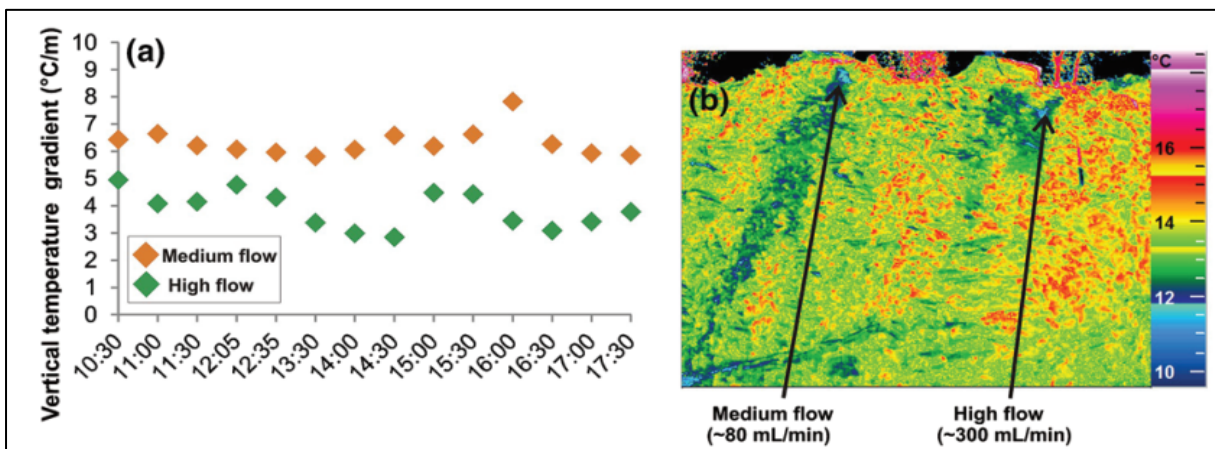


Figure 1.3 (a) An artificial seep experiment measuring the vertical temperature gradient for medium and high flows. On a qualitative level, the medium seepage exhibits a higher temperature than the higher seepage (b) A thermal image illustrating altered flow paths caused by the complexity of rocks surface.

Taken from Mundy (2017)

A laboratory test was conducted by Haack (1996), he used infrared thermography to locate a panel with different defects. Those defects were including one cavity and 3 moisture patches which were locating in different depths. The results showed that the defects with the area more than their depth (concrete covering) could be detected. His results show that infrared thermography is not applicable to find the dry cracks. The requirement for using infrared thermography successfully is the existence of a temperature gradient as 2 °C /meters through the tunnels (Haack et al., 1995). In order to get the proper results, the temperature measurements need to be continuous and conduct in certain points of shells along the tunnels. If a metal was used to cover the tunnels shell, the infrared thermography radiation would be shielded and that's not possible to detect the defects (Haack et al., 1995).

### **1.3.3 Advantages and limitations of infrared thermography**

There are many advantages of using thermography in brief:

- No physical contact required
- Non-destructive and effective
- Minimum operation intervention
- No harmful radiation
- Ease of interpretation of image
- Applied to almost all material and all components
- Cover a large area

Infrared thermography is associated with a number of limitations. Environmental factors have an impact on thermographic images and might make them difficult to obtain. Correct values of emissivity, specific heat, and humidity are required for the interpretation of the thermographic images (Lerma et al., 2011). Furthermore, measurements might be influenced by the texture of the corrected surface (Wimsatt et al., 2013).

Infrared thermography can estimate the area of the leakages surface; however, it cannot give a quantitative estimation (Lu et al, 2019). According to Mundy (2017), a solid quantitative relationship between groundwater flow rate and the vertical temperature gradient on the rock surface could not be obtained mainly because of various climate weather and complexities on the rock surface and flow direction. Irrespective of the limitations described above, under certain conditions, thermal imagery can be used to locate and characterize groundwater movement at seepage faces for examples when there is no solar radiation and no phase change and freezing (Mundy et al., 2017).

The infrared thermography considered a remote technique and consequently is limited by a variety of environmental and physical factors. For example, the measurements are confined to the surface water temperature. The groundwater seepage is found consistently, but only shallow systems (for example with depth of 0.5 metre) with moderate flow can be detected clearly (Hare et al., 2015).

By considering to this point that the thermograph images are more qualitative, using experimental modeling and numerical modeling are methods that can help to obtain more quantify results based on thermal images. To estimate the accurate quantitative relationships between the flow rate and temperatures, using an experimental simulation or numerical simulation is necessary. Their results can be compared with thermal images and finally find the possible correlation between different parameters.

M'nasri (2020) physical model of expansion joints allowed to investigate the temperature variation on the surface of the concrete due to different flow rate. The results of the studies performed on experimental model are summarized as follow:

- The temperature anomaly can be detected more clearly when a noticeable temperature difference exists between water and air.
- When comparing the most permeable joints to the others, they always record the highest temperatures in concrete.

- The infrared thermography measurement of flow rate across each joint clearly correlates with the intensity of temperature anomalies.
- As a function of time, temperature fluctuations at the joint and at the surface of concrete can be related to changes in flow rate.
- A model with increasing gap between air and water temperatures provides great contrast in the infrared thermography measurements (M'nasri, 2020).

#### **1.4 Numerical modelling**

Water infiltration at tunnel joints involves heat transfer and water seepage in porous media. Obtaining quantitative relationships between the joint parameters and temperature inside the tunnel would benefit from the development of a numerical model describing seepage and heat transfer close to the joint.

In porous media, heat and moisture transfer usually happens in a coupled system and involves a non-linear system. As a result, it is often challenging to develop precise numerical models for coupled heat and moisture transfer. Since the properties of porous materials are various, and they differ widely depending on the environment, the coupled equations are greatly nonlinear and solving them exclusively numerically is possible (Liu et al., 2013).

Researchers have created multiple models for the numerical modelling of seepage and heat transfer in porous media. These models have varying levels of complexity, and have different advantages and drawbacks (Wang et al., 2018). Mori et al., 2018 used a simple time-dependent heat transfer numerical model to study the temperature distribution of the Calgary airport trail tunnel. The temperature pattern of the cross-section of tunnels was simulated through time. Those results were analysed to improve the quality of thermal load designs in tunnels. More complex coupled models are used for building envelopes and walls. For example, to investigate the effect of moisture transfer on the temperature of the inner surface, Liu et al. (2013) used the temperature and relative humidity as driving potentials in a coupled model. The temperature of walls made from various materials was determined by using a coupled heat and moisture transfer transient model. The model was developed under constant and variable

boundary condition. Significant effect of moisture transfer on wall surface temperature was observed in the study by the researcher.

#### **1.4.1 Heat and moisture transfer**

Water infiltration include a complicated simultaneous heat and moisture transfer procedure. In order to study the effect of water infiltration in tunnels by infrared thermography, a deep understanding of this phenomenon is required. During water infiltration heat transfer happens between air, water and surrounding rock via conduction and convection. Moisture transfer happens through evaporation of water on the surface of the tunnels.

The heat exchange occurs between leaking water and air inside the tunnel by convection. This heat transfer depends on the flow rate and the velocity of water and the temperature difference of air and water inside the tunnel (Peltier et al., 2019). The heat and moisture transfer are controlled by relative humidity, evaporation and temperature difference of air and water temperature in tunnels (Li et al., 2021).

#### **1.4.2 Governing equations**

The mechanisms by which heat, and moisture are transferred through porous media are governed by two differential equations: the water conservation equation and the heat conservation equation in a porous environment.

#### **1.4.3 Water conservation equation in porous media**

For a temperature above 0 °C, the moisture flux in a porous media is composed of a vapor flux ( $J_v$ ) and a liquid flux ( $J_l$ ). The principle of mass conservation implies that these fluxes can be related to the water content ( $w$ ) of the porous media (Nilsson ., 2004):

$$\frac{\partial w}{\partial t} = -\nabla \cdot (J_v + J_l) \quad (1.3)$$

where  $\nabla$  is the divergence operator,  $w$  has units of  $\text{kg}\cdot\text{m}^{-3}$ , and  $J_l$  and  $J_v$  have units of  $\text{kg}\cdot\text{m}^{-2}\cdot\text{s}^{-1}$ . In general, the liquid and vapor fluxes follow the same direction, and it is often difficult to separate them in an experiment. As a result, the analysis of the two fluxes is sometimes combined (Nilsson ., 2004). In this project, we considered only the liquid flux and assumed that the concrete pores were saturated. Based on Darcy's law, the flux of water in the liquid state on a horizontal plane is governed by the following equation (Wang et al., 2021):

$$J_l = -\frac{k_l \rho_l}{\mu_l} \vec{\nabla} P_l \quad (1.4)$$

where  $\vec{\nabla}$  is the gradient operator,  $P_l$  is the pore water pressure ( $\text{Nm}^{-2}$ ),  $\rho_l$  is the water density ( $\text{kg}\cdot\text{m}^{-3}$ ),  $\mu_l$  is the water dynamic viscosity ( $\text{Pa}\cdot\text{s}$ ) and  $k_l$  is the concrete intrinsic permeability ( $\text{m}^2$ ), a property which describes how easily liquids flow in a porous media (e.g. Domenico & Schwartz 1998). The intrinsic permeability can be related to the hydraulic conductivity ( $K_l$ ), a property commonly used in geotechnical engineering which describes how easily a specific liquid flows in a porous media:

$$k_l = \frac{K_l \mu_l}{\rho_l g} \quad (1.5)$$

where  $g$  describe the acceleration of gravity ( $\text{m}\cdot\text{s}^{-2}$ ) and  $K_l$  has units of  $\text{m}\cdot\text{s}^{-1}$ . Equations 1.3 and 1.4 can be combined to obtain the following water conservation equation:

$$\frac{\partial w}{\partial t} = \nabla \cdot \left( \frac{k_l \rho_l}{\mu_l} \vec{\nabla} P_l \right) \quad (1.6)$$

For steady state conditions, the water content is constant and the partial derivative with respect to time on the left-hand side of equation 1.6 is equal to 0. In this case, the conservation equations take the following form:

$$\nabla \cdot \left( \frac{k_l \rho_l}{\mu_l} \vec{\nabla} P_l \right) = 0 \quad (1.7)$$

#### 1.4.4 Heat conservation equation in porous media

For steady state conditions, the heat conservation equation for porous media can be written as follows (Nield & Bejan, 2012):

$$\nabla \cdot (K_T \vec{\nabla} T) - \rho_l c_l J_l \cdot \vec{\nabla} T = Q_T \quad (1.8)$$

where  $K_T$  is the effective thermal conductivity of the porous media ( $\text{W} \cdot \text{m}^{-1} \cdot \text{K}^{-1}$ ),  $c_l$  is the heat capacity of water ( $\text{J} \cdot \text{kg}^{-1} \cdot \text{K}^{-1}$ ),  $\cdot$  is the dot product and  $Q_T$  is a local heat source ( $\text{J} \cdot \text{s}^{-1} \cdot \text{m}^{-3}$ ). The first term on the left-hand side is associated with conductive heat transfer while the second term is associated with advective heat transfer. Equation 1.8 assumes conditions of local temperature equilibrium, which means the temperatures of the liquid and solid phases are assumed to be equal. There is no difference in temperature between solids and fluids in steady conduction problems, under prescribed temperature conditions. Most problems involving a slow migration of water can be solved under the assumption of equal phase temperatures if volumetric internal heating does not vary between the two materials (Comsol, 2019).

The  $K_T$  value can be calculated from the thermal conductivity of the liquid ( $K_l$ ) and solid phases ( $K_p$ ). It is controlled by the geometry of the porous media in a complicated way. Based on the reciprocal average method, when heat propagates through both the solid and fluid phase in series, the effective thermal conductivity  $K_T$  can be calculated as the weighted harmonic average of  $K_l$  and  $K_p$ ,  $\theta_p$  is porosity of solid in porous medium (Comsol, 2019):

$$\frac{1}{K_T} = \frac{\theta_p}{K_p} + \frac{(1 - \theta_p)}{K_l} \quad (1.9)$$

Thermal conductivity of water is relatively high. The presence of water in a porous material increases its thermal conductivity. This greatly impacts the heat transfer within porous materials. For instance, the thermal conductivity of lime silica brick in the full saturation state is more than double the thermal conductivity in the unsaturated state (Dong et al., 2020).

A significant local heat source is the heat flux associated with evaporation and condensation. During the moisture adsorption–desorption process, the latent heat will transfer between porous media and the surrounding environment. This will lead to a local heating effect which is due to condensation, and a local cooling effect which is due to evaporation (Tariku et al., 2010). During water evaporation from a concrete surface, latent heat is discharged from the water. This process causes a temperature drop on the concrete surface. Observations show that ignoring latent heat can lead to significant errors in the prediction of air temperature in tunnels (Li et al., 2021). The amount of heat necessary for evaporation is depends on the evaporation rate. The evaporation rate depends on the temperature difference of water and air, and most importantly relative humidity. Infiltrated water moves to the surface of the tunnels through joints. Part of the water evaporates and part of the water seeps on the surface of the tunnel. These proportions depend on the relative humidity, and the air and water temperature.



## **CHAPTER 2**

### **METHODOLOGY**

In this project, a numerical model of coupled heat and moisture transfer was created to simulate the temperature and pore pressure close to an expansion joint in concrete. The model was calibrated with experimental data obtained by M'nasri (2020) with a physical model. The numerical model was created using COMSOL, a finite element code. This chapter introduces the physical and numerical models.

#### **2.1 Physical model**

The construction of the physical model was described in detail by M'nasri (2020). A laboratory physical model was built based on the expansion joints of the Ville-Marie tunnel. This model was utilized to investigate the effect of groundwater temperature changes on the concrete temperature close to a series of expansion joints with different permeability. The objective was to generate experimental data to study the relationship between joint permeability, flow rate and temperature at the concrete surface based on infrared thermography.

##### **2.1.1 Description and construction of the physical model**

Figure 2.1 present the model schematically. The model was made of unreinforced concrete. It has the shape of a rectangular prism with dimension of 45 cm by 60 cm. The model is empty at the center. The center of the model was filled with water simulating groundwater outside the tunnel. The outside of the model represents the situation inside the tunnel.

An expansion joint was constructed on each vertical side of the model. The joints were made with different materials to create different permeability. The reference joint was made of a polystyrene (XPS type) sheet with a PVC water stop. The second joint was made of a polystyrene sheet without a water stop. Thin sheets of extruded polystyrene were used for the

third joint to increase the permeability. The fourth joint was initially filled with cement-bentonite grout with a specific permeability, but was later replaced with a single polystyrene sheet sealed with silicon. The cement-bentonite grout had to be removed because it dried and became brittle. The thickness of each joint was 2.54 cm. Figure 2.2 shows the fourth joint, the joint that was simulated with the numerical model in this project.

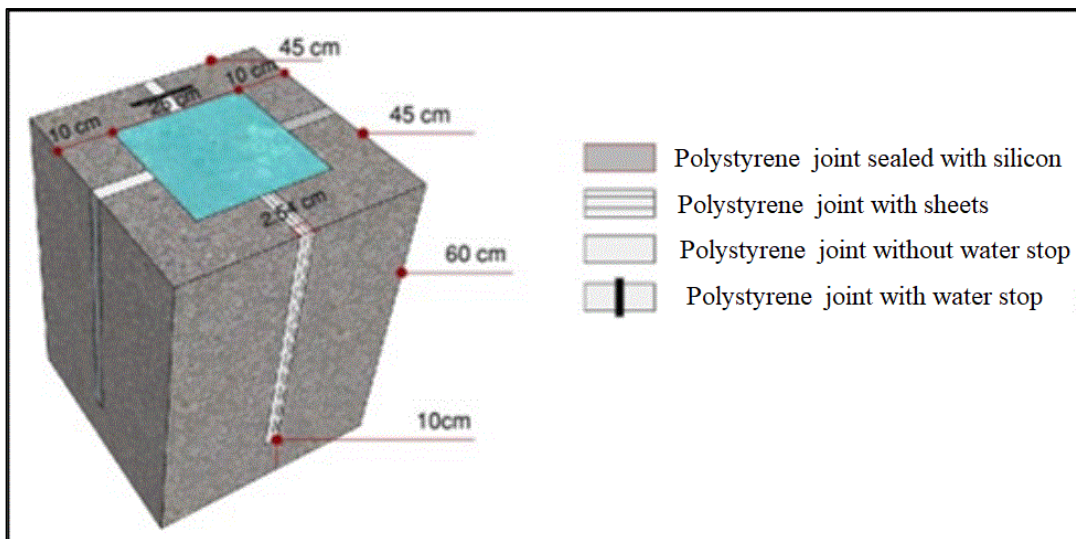


Figure 2.1 Diagram of the physical model of the expansion joints  
Adapted from M'nasri (2020)

The concrete mix was designed to have a compressive strength greater than 30 MPa. Two permeability tests were performed on the concrete according to the standard ASTM D5084 (ASTM International 2016). A mean hydraulic conductivity of  $4.2 \times 10^{-12}$  m/s was obtained for water at 20 °C.

In order to determine the temperature change within the concrete along its thickness, two sets of thermocouples were installed at a distance of 5 and 10 cm from each joint at depths of 3 and 7 cm. The position of the thermocouples with respect to the expansion joints is shown in Figure 2.2 for the joint that was modeled in this project. The thermocouples were calibrated before being installed at the proper location. The temperatures obtained with the 16 thermocouples were recorded with an acquisition card and a LabVIEW program (Figure 2.3).

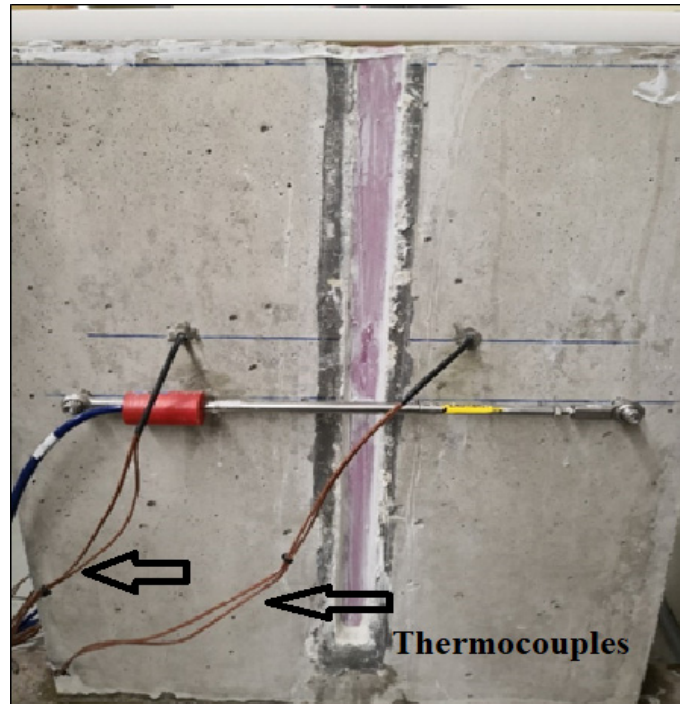


Figure 2.2 A surface of physical model of the Expansion joints Taken from M'nasri (2020)

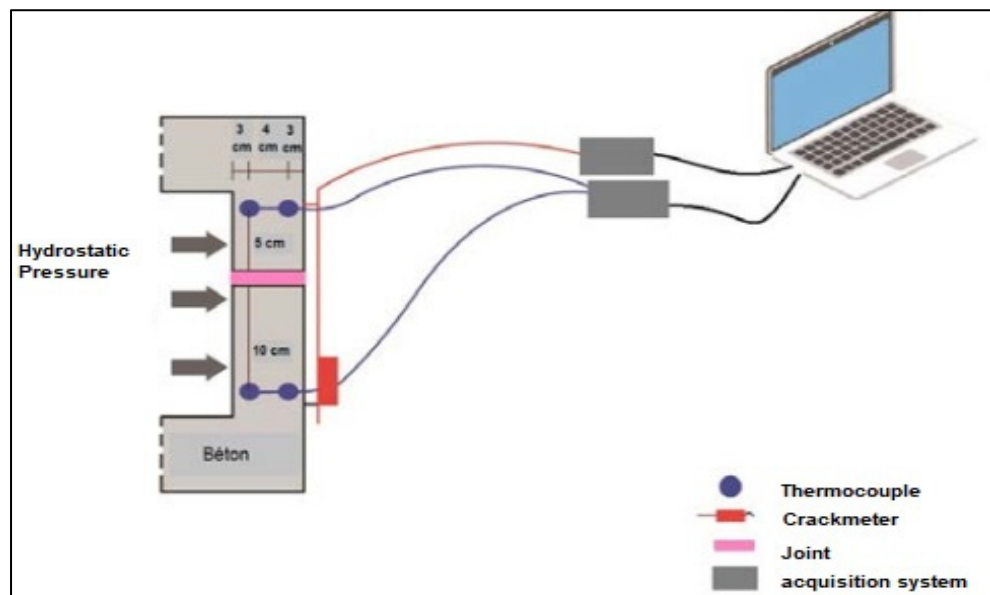


Figure 2.3 Arrangement of thermocouples and data acquisition Taken from M'nasri (2020)

### 2.1.2 Test procedure

The test was conducted in two stages. Water in the model was kept at room temperature for the first stage and it was cooled to a minimum temperature of 12 °C for the second stage. Both phases lasted 6 hours. The assembly had two pipes. The water flows through the first pipe to the assembly. The circulation of water took place via the second pipe. The water circulation is shown in Figure 2.4. The first phase of the test consisted of the circulation of water from basin 1 to the bottom of the PVC column and then to the assembly (Figure 2.4).

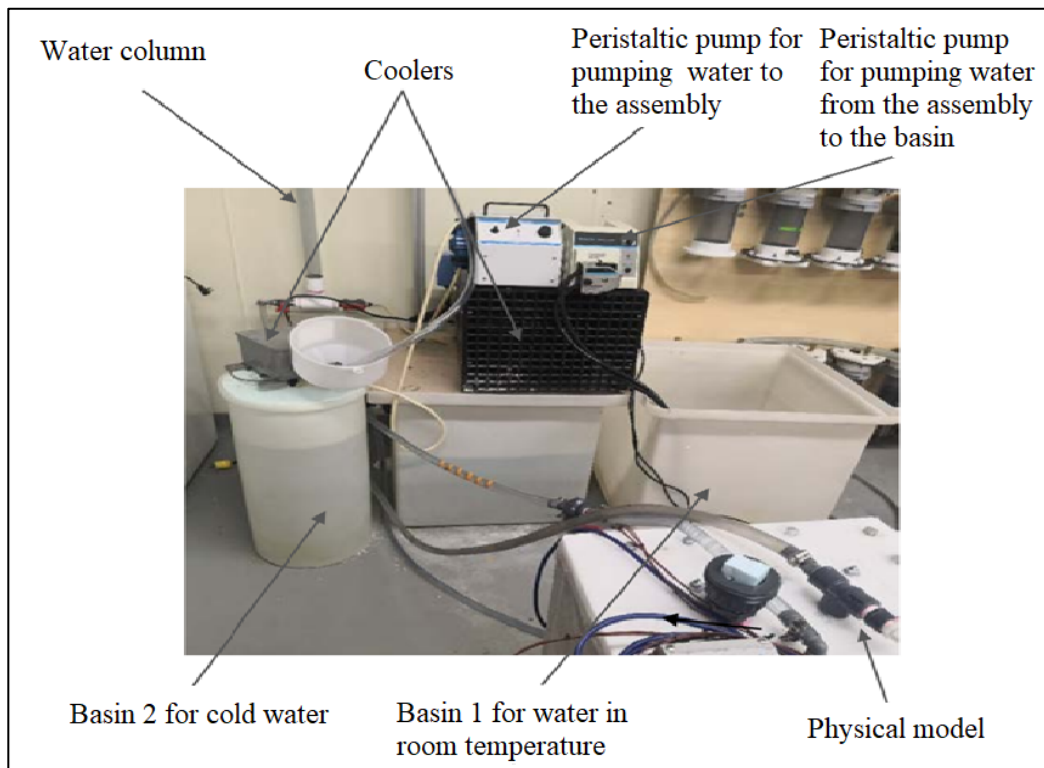


Figure 2.4 Water circulation for two phase of tests  
Adapted from M'nasri (2020)

The water column serves as a shock absorber. By using it, the water level in the assembly could be maintained and the flow to the assembly was regulated. Pumping of the water was carried out by the left peristaltic pump. A certain part of the water was cooled in basin 2 by the chiller

in Figure 2.4 before phase 1 was completed. In order to begin phase 2, the channel of peristaltic pump has been transferred from basin 1 to basin 2. A peristaltic pump is shown at the right side in Figure 47. It was pumping water from the center of the assembly toward basin 1, in order to ensure that the water change occurs as quickly as possible. In the first hour of each phase, flow measurements were conducted every 15 minutes and thereafter every hour. In order to calculate the flow rates, the weight of water in each gutters was measured (Duhaime et al., 2019).

The thermal images for each joint were captured using an infrared camera model FLIR E64501. In order to have similar acquisition conditions and a constant scale for each image, the distance between the model surface and the camera was fixed at 1.73 m.

## **2.2 Numerical model**

The numerical model was developed with the finite element code COMSOL Multiphysics. This section presents the geometry, the mesh and the differential equations that were solved.

### **2.2.1 Geometry and mesh**

Figure 2.5 shows the geometry of the numerical model. The model corresponds to a plan view (horizontal section) of the physical model. A complete horizontal section is modeled to take into account the geometry of the physical model, but only one joint is modeled in the blue domain in Figure 2.5. Modelling the complete section allows to simulate the influence of the corners of the model. The dimension of the blue subdomain is  $0.1 \times 0.45$  m. The dimension of the joint is  $0.1 \times 0.0254$  m. The expansion joint is made of expanded polystyrene and the other parts is made of concrete. As part of the COMSOL modeling process, a physics-controlled mesh was used to create the mesh based on the geometry of the model. The element size was set to extremely fine and 5778 triangular elements were used. Temperature equations were solved using linear interpolation functions and pressure functions were solved using quadratic equations. The results were independent to mesh.

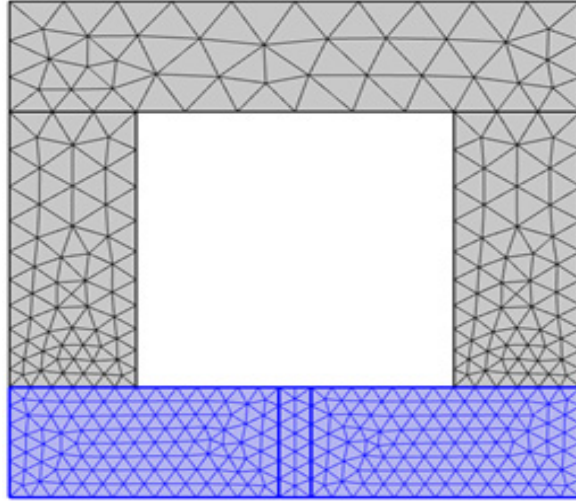


Figure 2.5 The model domain in this study

### 2.2.2 Governing equations and boundary conditions

The numerical model is centered on the water conservation equation and heat conservation equations that were presented in chapter 1 (Equations 1.7 and 1.8). A steady-state simulation was used. This assumes that the model has reached equilibrium. In terms of the physical model presented by M'nasri (2020), this correspond to the end of the different test stages.

The theoretical model is simplified based on the following assumptions:

- The porous material has uniform properties.
- The solid, liquid, and gas phases in the concrete and polysatyrene are at a local thermal equilibrium.
- There is a pressure equilibrium in the liquid and gas phases.
- Gravity has little effect on a body.
- Water remains well below the boiling point.
- Ice formation and melting are ignored.
- The concrete and the dilatation joint are modeled as porous material but with different porosities.

A custom boundary condition had to be created and programmed in COMSOL for the concrete surface in the tunnel. The heat flux at the concrete surface has two components associated with the convection and evaporation mechanisms. The heat flux due to convection is expressed as follows (Wang et al., 2018)

$$Q_c = h_c(T_{air} - T_{concrete}) \quad (2.1)$$

where  $h_c$  is the convection coefficient in  $W/(m^2.K)$ ,  $T_c$  represents the concrete surface temperature and  $T_{air}$  is the air temperature in K. Heat flux due to evaporation can be expressed as follows based on the assumption that the flow rate is completely evaporated at the concrete surface (Liu et al., 2013):

$$J_v = \nabla h_v \rho_w K_{concrete} \frac{\delta h}{\delta y} \quad (2.2)$$

where  $\Delta h_v$  is the latent heat of water evaporation in J/kg,  $\rho_w$  is the density of water,  $K_{concrete}$  is the hydraulic conductivity of concrete, and  $\partial h/\partial y$  is the hydraulic gradient at the concrete surface.  $\Delta h_v$  is defined as the energy required to vaporize 1 kg of water. It can be expressed as follows (Liu et al., 2013):

$$\Delta h_v = (2500 - 2.4T_{air}) \times 10^3 \quad (2.3)$$

Equation 2.2 should be limited by a maximum evaporation rate. For higher flow rates, only some part of the seeping water can be evaporated. The rest of the infiltrated water will seep down the concrete surface. The heat flux due to evaporation of maximum flow rate can be defined based on equation 2.4 (Liu et al., 2013):

$$J_v = 610.5 \frac{\Delta h_v h_c}{R_v \rho_a c_p} \left( \frac{h_v \exp\left(\frac{17.269T_{air} - 4717}{T_{air} - 35.85}\right)}{T_{air}} - \frac{\exp\left(\frac{17.26T_c - 4717}{T_c - 35.85}\right)}{T_c} \right) \quad (2.4)$$

Where  $R_v$  is the gas constant for water in vapour condition  $462 \text{ J.kg}^{-1}\text{K}^{-1}$ ,  $\rho_a$  is the density of air  $1.204 \text{ kg.m}^{-3}$  ( $20 \text{ }^\circ\text{C}$  and  $101.3 \text{ kPa}$ ) and  $c_p$  is the thermal mass capacity  $1005 \text{ (J kg}^{-1} \text{ K}^{-1})$ ,  $h_r$  describe relative humidity and  $T_C$  is concrete temperature.

The total heat flux for the situation in which the flow rate is more than the maximum evaporation rate is defined by equation 2.5:

$$Q_{Total} = h_c(T_C - T_{air}) + 610.5 \frac{\nabla h_v h_c}{R_v \rho_a c_p} \left( \frac{h_r \exp\left(\frac{17.269 T_{air} - 4717}{T_{air} - 35.85}\right)}{T_{air}} - \frac{\exp\left(\frac{17.26 T_C - 4717}{T_C - 35.85}\right)}{T_C} \right) \quad (2.5)$$

When the Darcy velocity is less than the maximum evaporation rate, the heat flux boundary condition at the concrete surface is expressed as equation 2.6 :

$$Q_{Total} = h_c(T_C - T_{air}) + \Delta h_v \rho_w K_{concrete} \frac{\delta h}{\delta y} \quad (2.6)$$

For both equations, the first term account for convection and the second term accounts for evaporation. Figure 2.6 shows the utilization of each equation in the simulation.

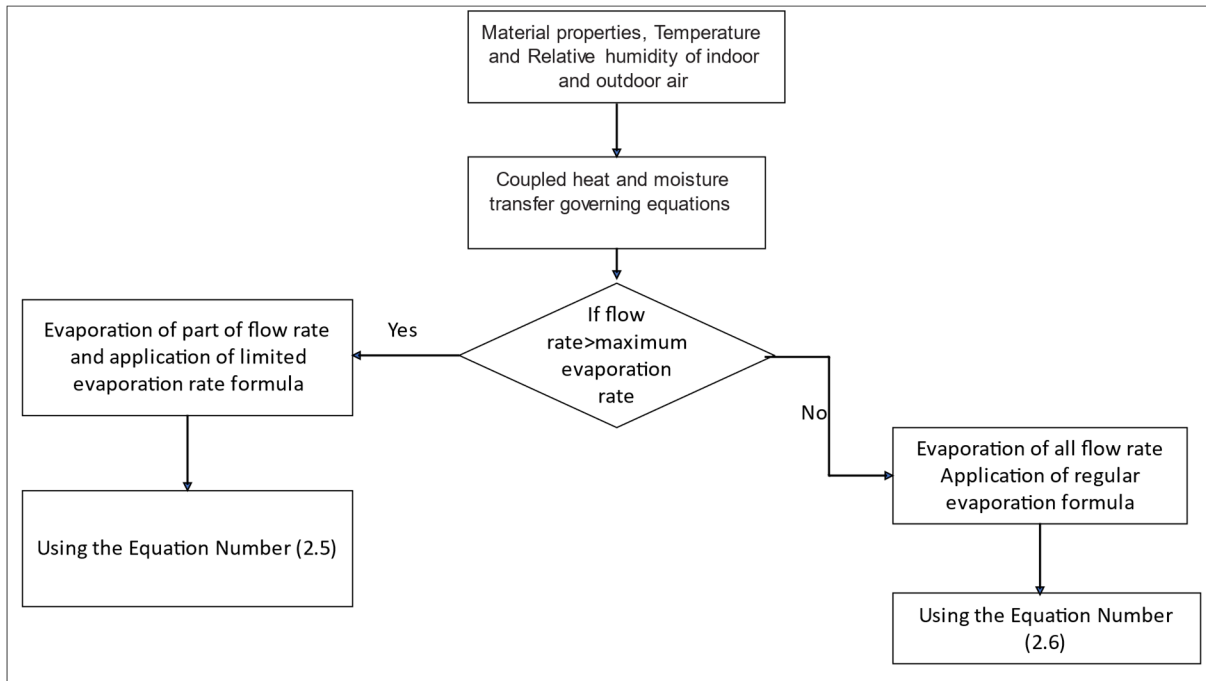


Figure 2.6 Flowchart for the flux boundary condition at the concrete surface.

For a base condition, the initial temperature of water is assumed to be same as groundwater temperature in Montreal, which is approximately 13 °C (Duhaime et al., 2019). The air temperature is assumed to be 20.5 °C. Water pressure ( $P_l$ ) of central part of the model (which represent outside of the tunnel) assumed to be equivalent to average pressure for a water height of 0.25 meters ( $h$ ). The 0.25 m water column is measured base on the dimension of the physical model. This pressure represents the boundary condition of the underground side of the tunnels and calculated according to equation 2.6 (Comsol, 2019):

$$P_l = \rho_l g h \quad (2.6)$$

where  $g$  is the acceleration of gravity ( $9.8 \text{ m}\cdot\text{s}^{-2}$ ) and  $\rho_l$  is density of water. After substitution those values, water pressure as of 2.45 kPa was calculated as boundary condition for water pressure.

In this model, the water density was assumed constant as it has a negligible influence on the results. The influence of water dynamic viscosity ( $\mu_l$ ) is relatively small as well. The water dynamic viscosity is a function of temperature and describes as follows:

$$\mu_l = (2.1 \times 10^{-6}) \exp\left(\frac{1808.5}{273.15+T}\right) \quad (2.7)$$

In this equation, T is the water temperature in °C and  $\mu_l$  is the dynamic viscosity in Pa·s. The hydraulic conductivity ( $K_l$ ) of concrete and expansion joints was considered  $10^{-12}$  m/s and  $10^{-7}$  m/s respectively for a base condition. According to equation 1.5, their corresponding intrinsic permeability ( $k_l$ ) are given in table 2.1:

Table 2.1 Intrinsic permeability values ( $k_l$ )

Concrete permeability (m <sup>2</sup> )	Joint Permeability (m <sup>2</sup> )
$1.04 \times 10^{-19}$	$1 \times 10^{-14}$

Outside the physical model, at the concrete surface, the water pressure is equal to zero, or atmospheric pressure. The heat flow boundary condition outside the model combines convection and evaporation as explained previously. Figure 2.7 summarizes the boundary conditions for the expansion joint model.

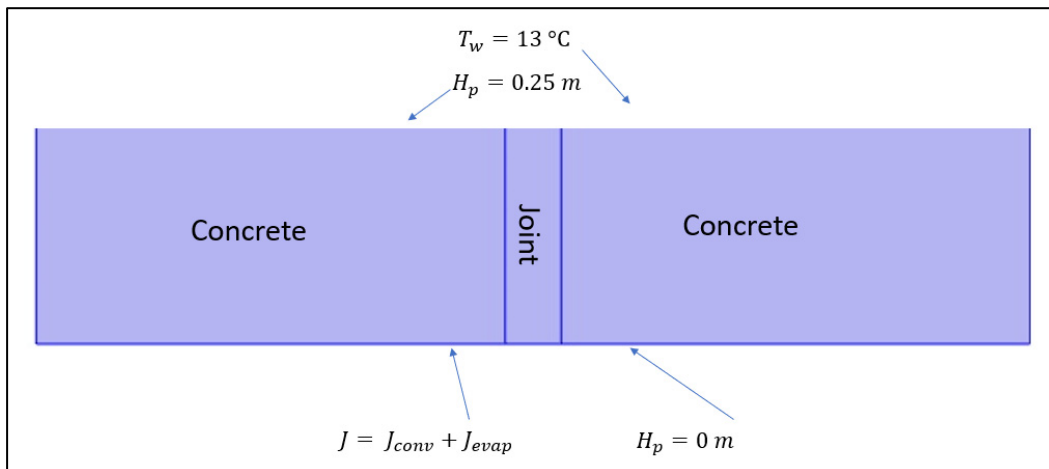


Figure 2.7 Summary of boundary conditions on the model

### 2.2.3 Parametric study

The parameter values given in the previous sections were used to validate the numerical model based on the experimental results presented by M'nasri (2020). A parametric study was also conducted to verify the influence of each parameter. The water and air temperature, joint permeability, humidity, and convection coefficient were varied to investigate their influence on the temperature and heat flux profiles. Table 2.2 show the range of values taken by each parameter.

Table 2.2 List of parameter values

Parameters	Values
Air temperature (°C)	5, 10, 25, 20.5
Water temperature (°C)	5, 10, 13, 15
Convection coefficient (W/(m <sup>2</sup> ·K))	1, 3, 3.5, 10
Joint permeability (m <sup>2</sup> )	1×10 <sup>-19</sup> , 3×10 <sup>-19</sup> , 5×10 <sup>-19</sup> , 1×10 <sup>-18</sup> , 3×10 <sup>-18</sup> , 5×10 <sup>-18</sup> , 1×10 <sup>-17</sup> , 3×10 <sup>-17</sup> , 5×10 <sup>-17</sup> , 1×10 <sup>-16</sup> , 3×10 <sup>-16</sup> , 5×10 <sup>-16</sup> , 1×10 <sup>-15</sup> , 3×10 <sup>-15</sup> , 5×10 <sup>-15</sup> , 1×10 <sup>-14</sup> , 3×10 <sup>-14</sup> , 5×10 <sup>-14</sup> , 1×10 <sup>-13</sup> , 3×10 <sup>-13</sup> , 5×10 <sup>-13</sup>
Concrete permeability (m <sup>2</sup> )	1.0204×10 <sup>-14</sup>
Relative humidity (-)	0.45, 0.56, 0.78, 0.99



## CHAPTER 3

### RESULTS AND DISCUSSION

In this chapter, the numerical model is first validated and calibrated with the experimental results of M'nasri (2020). The second part of the chapter presents the results of a parametric study. Parametric studies were conducted to verify the influence of the numerical model parameters on the temperature and heat flux profiles at the concrete surface. The last section of the chapter looks at the temperature anomaly at the joint.

#### 3.1 Model validation and calibration

In this section, the numerical results are compared with the experimental results of M'nasri (2020) to validate the model and to calibrate the model with the convection coefficient and the joint permeability two parameters that cannot be obtained independently.

As explained in chapter 2, the experimental model was run in two phases. In the first phase, the water temperature was 20 °C and the air temperature was 20.5 °C. For the second phase, the water was cooled to 12 °C and air was kept in same temperature (20.5 °C).

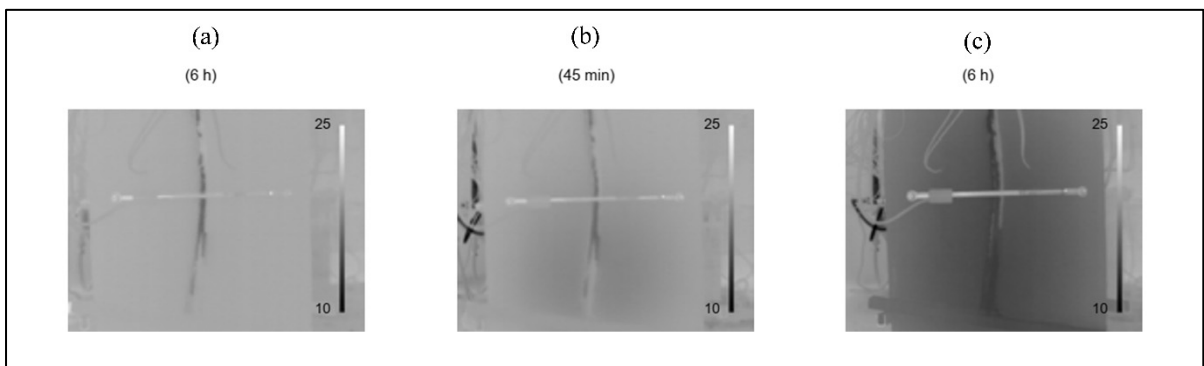


Figure 3.1 Three series of infrared thermographs. The first one was taken at the end of the first phase (a), the second one was taken 45 minutes after the start of the second phase (b) and the third one was taken at the end of the second phase (c)

Taken from M'nasri (2020)

For temperature calculations, the air temperature and emissivity were 20.5 °C and 0.9, respectively. The darker areas correspond to lower surface temperatures. Temperature anomalies related to water infiltrations can be observed in Figure 3.1 (a) even if the water and air temperatures are equal. The evaporation of water creates a temperature anomaly. Since water takes energy to transfer from the liquid phase to the gas phase.

Figure 3.1 (c) shows the anomaly at the end of phase 2 is more significant at the bottom of the joint in comparison to phase 1. The three thermographs are showing the same joint. Therefore, it is clear that the difference between water and air temperature significantly influences the temperature patterns. The joint permeability is not the only factor influencing the temperature anomaly.

The numerical model was calibrated using the temperatures at the end of the two phases on the joint. The temperatures on the joint surface and 5 cm away from the joint on the concrete obtained from infrared thermography measurements were used for calibration, along with the four temperatures recorded by the four thermocouples inside the model. The calibration was done for steady-state conditions at the end of each phase. The air temperature (20.5 °C), the water temperature (12 °C or 20 °C depending on the test phase), and the relative humidity (0.56) were set for calibration. The calibration was done by changing the joint permeability and the convection coefficient until reaching the same results as obtained for experimental model results. The values of  $h_c = 3.5 \text{ W}/(\text{m}^2 \cdot \text{K})$  and joint permeability of  $1 \times 10^{-14} \text{ m}^2$  let to produce the same results of the temperature measured by M'nasri (2020). The calibration is shown in Figure 3.2. This set of parameters resulted in the best fit between the numerical and experimental results.

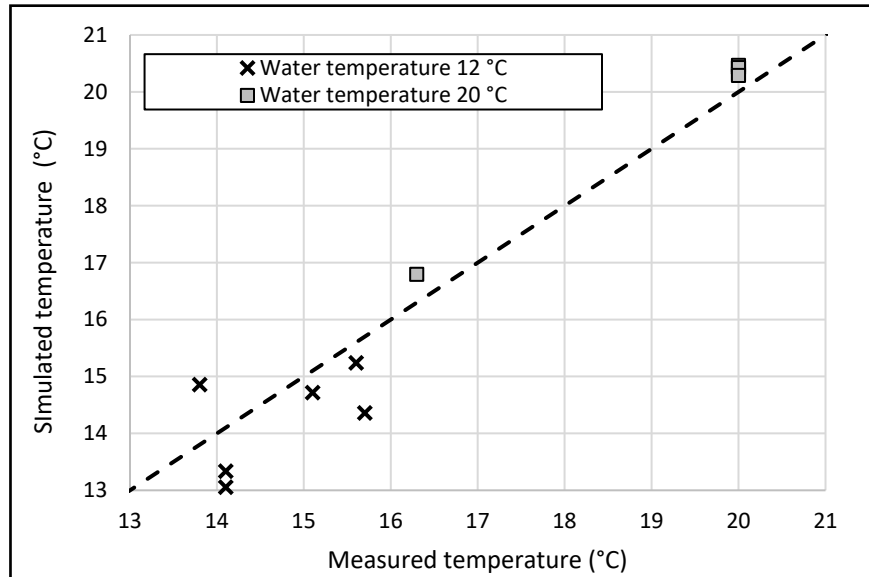


Figure 3.2 Temperature calibration for the numerical model based on the experimental results presented by M'nasri (2020)

Figure 3.3 shows 2D temperature corresponding to the two-phase numerical model. Figure 3.3 (a) shows the 2D temperature grid for water temperature 20 °C and air temperature 20.5 °C. As you can see from the picture, for this phase as the water temperature is equal to air temperature, the temperature grid is relatively constant. The temperature inside concrete model is 20.5 °C which has shown with lighter colour in bar grid. The temperature decreases only observe on the joint area, due to evaporation effect. It is shown in darker colour, and is around 16.97 °C.

Figure 3.3 (b) shows 2D temperature grid for the second phase (water temperature and air temperature are 12 °C and 20.5 °C respectively). For second phase the temperature difference are noticeable in different part of model due to difference between water and air temperature. As it can be seen, the darker or lower temperatures are far from the surface of concrete. These areas are closer to the groundwater temperature which is in centre part of model. The minimum temperature is as of 12 °C.

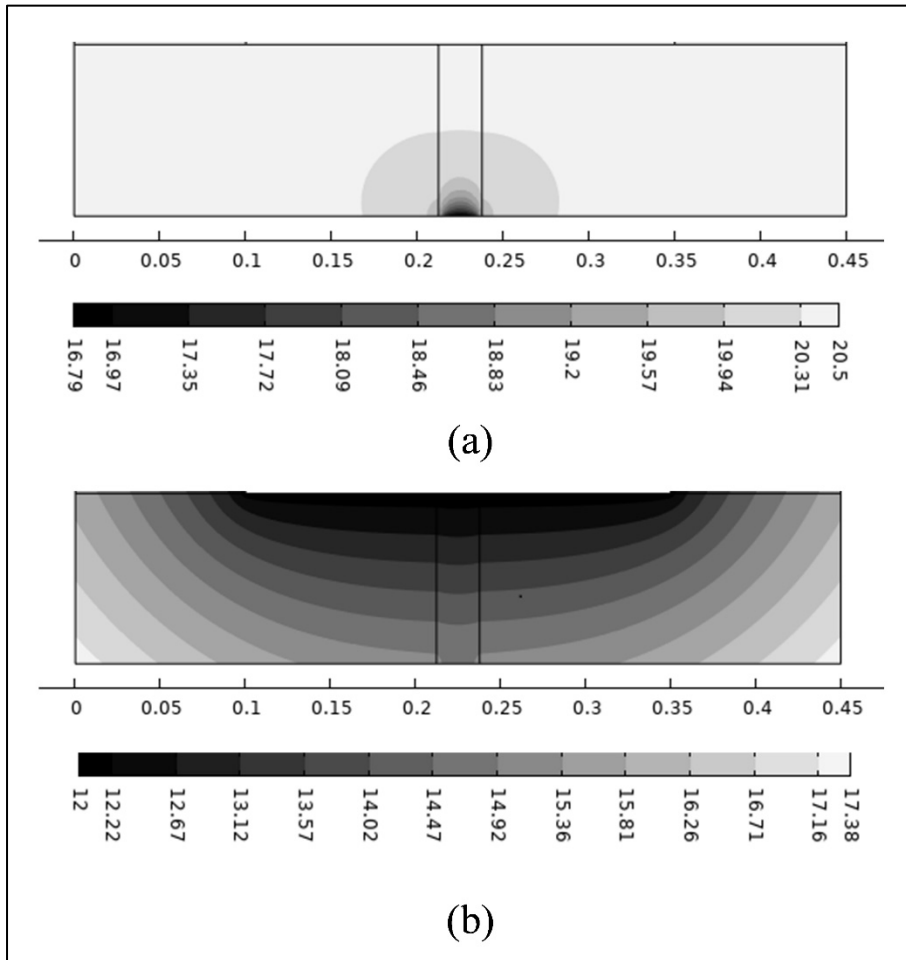


Figure 3.3 2D section of the model with temperature colour grid.  
 (a) For water temperature 20 °C and air temperature 20.5 °C  
 (b) For water temperature of 12 °C and air temperature 20.5 °C

Figure 3.4 shows a comparison between the concrete and joint surface temperature obtained from the numerical model and obtained from the physical model by M'nasri (2020). The temperature for the physical model was obtained using infrared thermography on a horizontal line situated approximately at the model mid height. As it can be seen, the temperature trends are similar. The main difference is the small positive anomaly on the right side of the joint for the physical model with  $T_{water} = 12$  °C. This positive anomaly can also be seen in Figure 3.1(c)

as the pale grey colour on the right side of the joint at the mid height of the model. This positive temperature anomaly could be due to a difference between the emissivity of concrete between dry polystyrene and wet polystyrene. The surface temperature with infrared thermography was calculated based on a constant emissivity for concrete and polystyrene. These materials probably have different emissivity values.

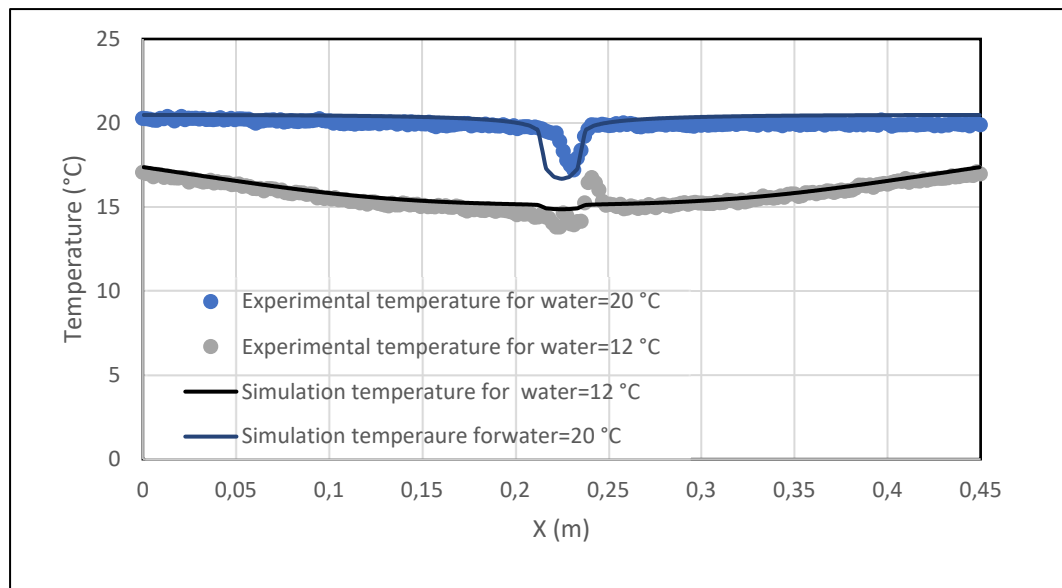


Figure 3.4 Comparison between the surface temperature measured by M'nasri (2020) on the physical model and the numerical model results for an air temperature of 20.5 °C

### 3.2 Parametric study

During the parametric study, each property was varied separately while maintaining the other constant. The reference value for each property is presented in Table 3.1.

Table 3.1 Reference values for the parameters

Air temperature (°C)	Water temperature (°C)	Convection coefficient (W/(m <sup>2</sup> ·K))	Relative humidity (-)	Joint permeability (m <sup>2</sup> )
20.5	13.0	3.5	0.70	1×10 <sup>-15</sup>

Two main types of graphs are introduced in this section; temperature profiles, heat flux profiles and a third type of graph which are temperature anomaly graphs, will be presented in the next section. The horizontal axis on the temperature and heat flux graphs shows the X coordinate. The joint is located between  $X = 0.2123$  m and  $0.2377$  m along this axis. The corners of the square model are located at  $X = 0$  and  $X = 0.45$  m.

### **3.2.1 Relative humidity**

Figures 3.5 and 3.6 show the influence of relative humidity on the temperature and on the heat flux at the concrete surface, respectively. It can be noticed that a higher relative humidity leads to a higher temperature on the joint. This is due to the relationship between relative humidity and the maximum rate of evaporation. A lower relative humidity leads to a higher evaporation rate and a lower temperature at the joint surface. Therefore, a joint leaking in a higher relative humidity environment will have a higher temperature. Figures 3.6 also shows for higher relative humidity, the total heat flux is greater (based on the direction of the total heat flux). These results clearly demonstrate that the temperature anomaly along the concrete surface depends on atmospheric conditions.

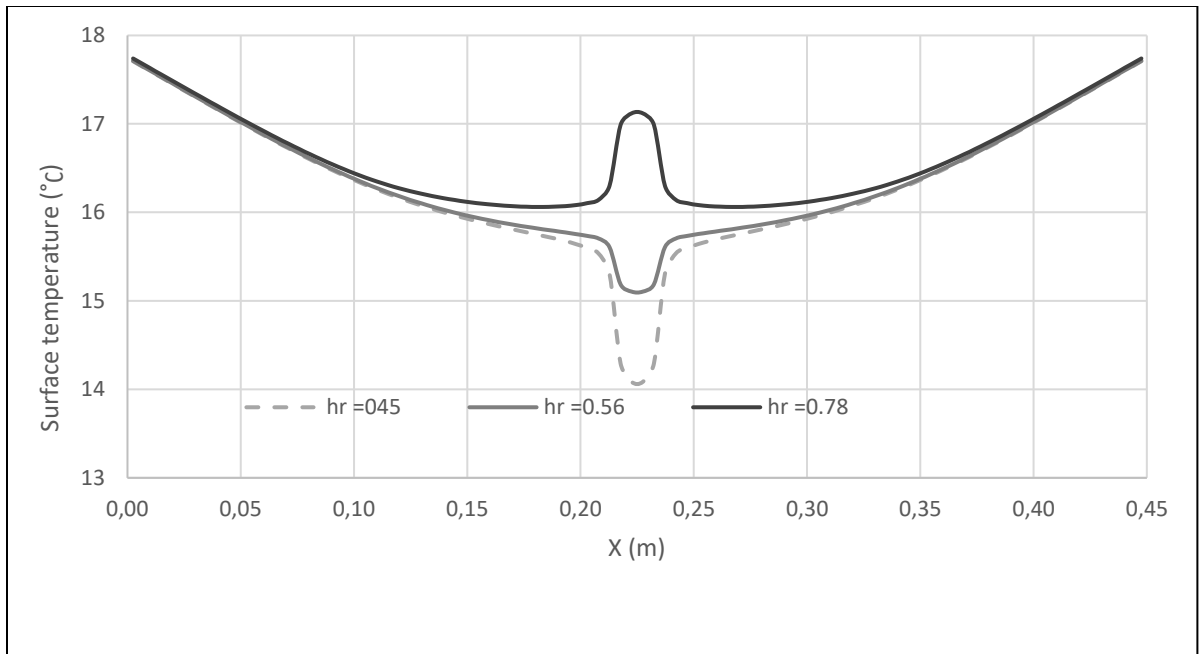


Figure 3.5 Influence of relative humidity on temperature at the concrete surface for  $T_{water}=13\text{ }^{\circ}\text{C}$  and  $T_{air}=20.5\text{ }^{\circ}\text{C}$

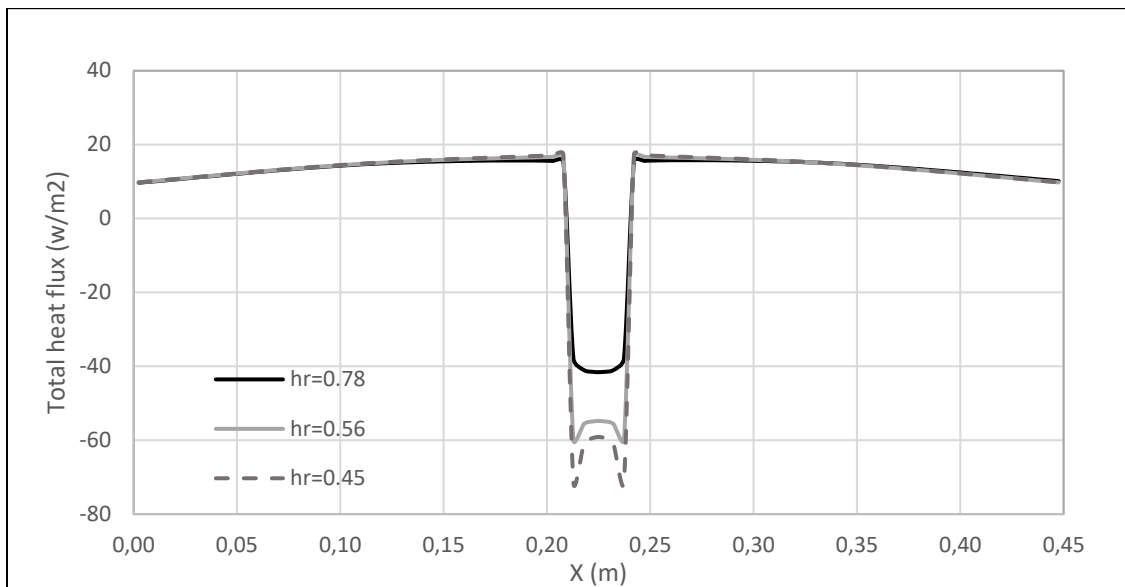


Figure 3.6 Influence of relative humidity on the total heat flux component at the concrete surface for  $T_{water}=13\text{ }^{\circ}\text{C}$  and  $T_{air}=20.5\text{ }^{\circ}\text{C}$

### 3.2.2 Air and water temperatures

Figures 3.7 and 3.8 were plotted to investigate the influence of changing the water and air temperatures on the concrete surface temperature. The other properties were set to the reference values in Table 3.1. For both Figure 3.7 and 3.8, the gradual temperature change away from the joint (toward 0 and 0.45 m) is due to the corners of the model. The temperature variation along the surface occurs with the difference between the water and air temperatures. The temperature variation is not 0 for a temperature difference of 0 between water and air temperature. For example, Figure 3.7 demonstrate the temperature between concrete and joint surface does not change for air temperature 22.75 °C and water temperature of 13 °C (the red curve). The red curve shows the position that the temperature difference along the surface of concrete is relatively constant.

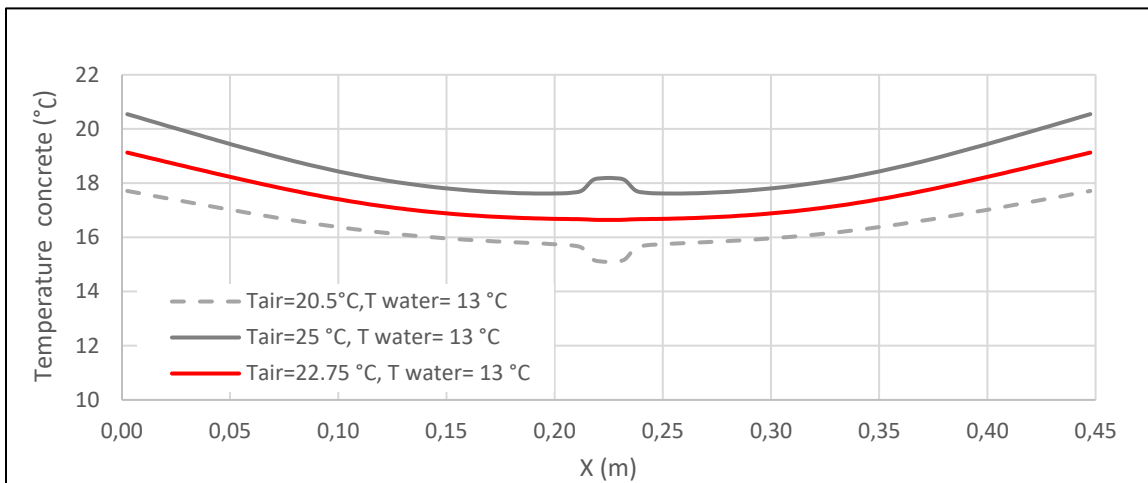


Figure 3.7 Influence of air temperature on the concrete surface temperature for  $T_{water} = 13 \text{ }^{\circ}\text{C}$

For Figure 3.8 the red curve shows the temperature difference along the surface of concrete is relatively constant for a water temperature 11.5 °C and air temperature of 20.5 °C.

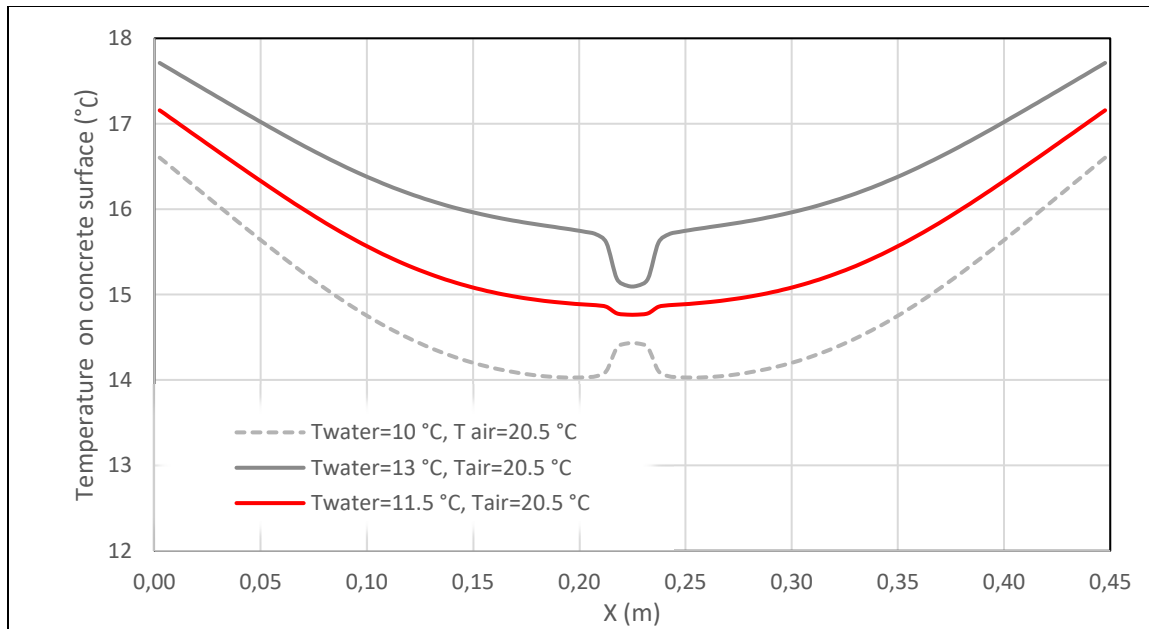


Figure 3.8 Influence of water temperature variation on the temperature on the surface of the concrete for  $T_{air}=20.5^{\circ}\text{C}$

The influence of air and water temperatures on the surface temperature can be understood in terms of the components of heat flux at the heat surface. Figure 3.9 shows the heat flux components at the concrete surface for the base conditions ( $T_{water} = 13.0^{\circ}\text{C}$  and  $T_{air} = 20.5^{\circ}\text{C}$ ). The two heat flux components (convection and evaporation) are plotted with the total heat flux and the maximum evaporation heat flux based on the total evaporation of the flow rate determined based on Darcy's law. The total heat flux is the sum of the heat flux due to evaporation and the heat flux due to convection. A positive heat flux enters the model and propagates in the concrete through conduction. For base conditions, on the joint, the heat flux due to evaporation is of the same order as the convection, but in opposite direction. Therefore, the total heat flux on the joint is close to zero. It should be noticed that the maximum evaporation is a limiting factor for joint in this case. The heat flux due to complete water evaporation is more than twice the real heat flux due to evaporation. This implies that a significant part of the water outflow at the joint surface would leave the system and trickle downward on the joint surface as the evaporation rate is not high enough. There is almost no evaporation on the concrete surface because the permeability is very low. As a consequence,

the total heat flux on the concrete is equal to the convection component. As a result, convection is the controlling factor in heat transfer process on concrete.

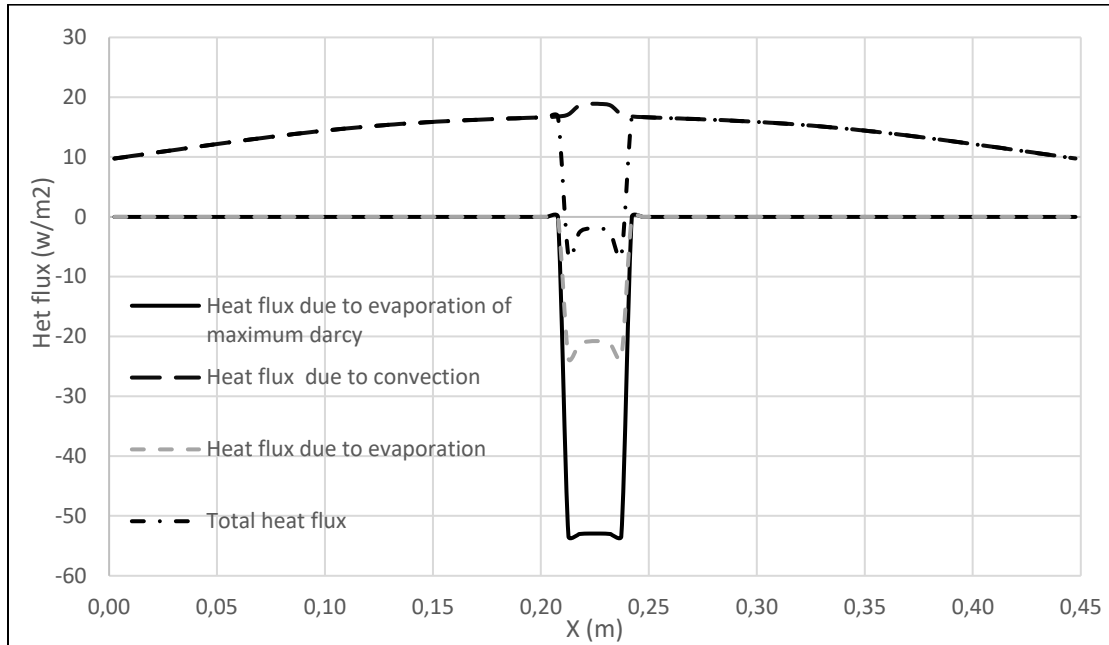


Figure 3.9 Heat flux components for  $T_{\text{air}} = 20.5 \text{ }^{\circ}\text{C}$  and  $T_{\text{water}} = 13 \text{ }^{\circ}\text{C}$

Figure 3.10 shows the components of heat flux for  $T_{\text{water}} = 5 \text{ }^{\circ}\text{C}$  and  $T_{\text{air}} = 25 \text{ }^{\circ}\text{C}$ . The total heat flux on the joint is positive as the convection is positive and greater than evaporation. On the concrete, the total heat flux is positive as well. For the concrete and joint, both evaporation and convection are controlling factors.

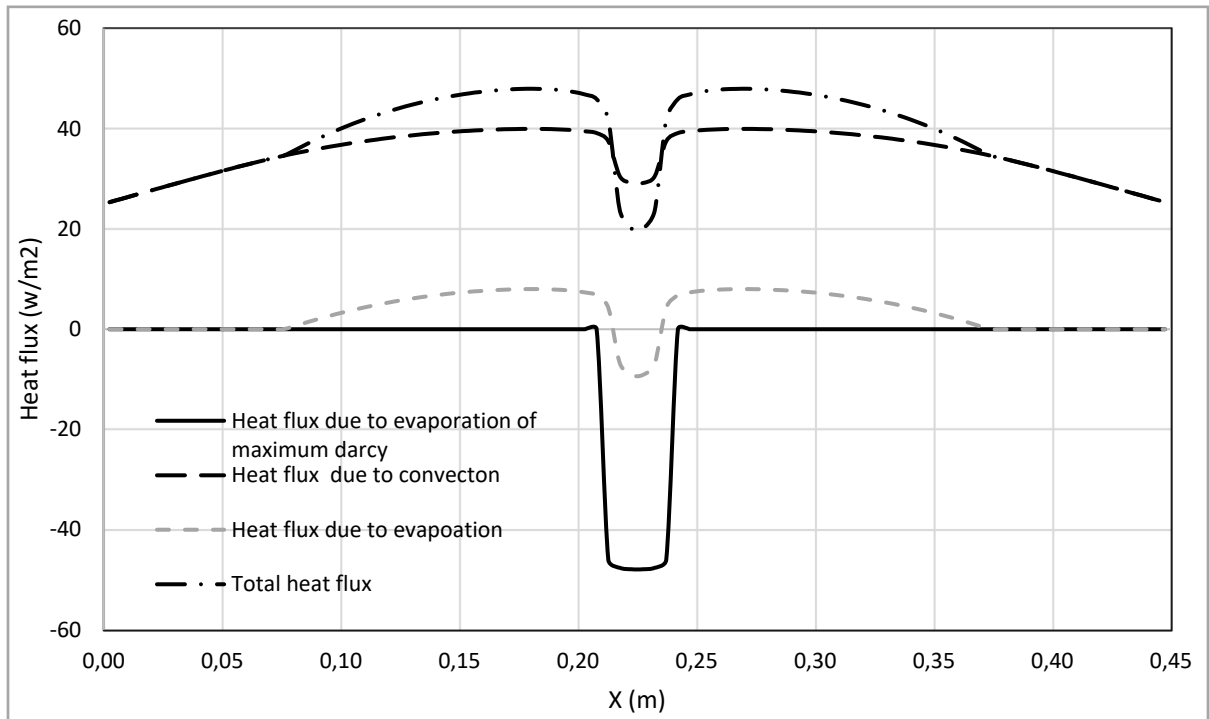


Figure 3.10 Heat flux components for  $T_{\text{air}} = 25 \text{ }^{\circ}\text{C}$  and  $T_{\text{water}} = 5 \text{ }^{\circ}\text{C}$

Figure 3.11 shows the different component of heat flux for the reverse situation in which the water is warmer than air temperature ( $T_{\text{water}} = 15 \text{ }^{\circ}\text{C}$  and  $T_{\text{air}} = 5 \text{ }^{\circ}\text{C}$ ). In this case, the total heat flux is negative on the joint, as there is a heat loss due to evaporation. As the air temperature is less than water temperature, the system also loses heat through convection from the joint to the air. The total heat flux is also negative on the concrete surface and controlled by convection. Because there is no evaporation on the concrete, the total heat flux is controlled by the convection heat flux.

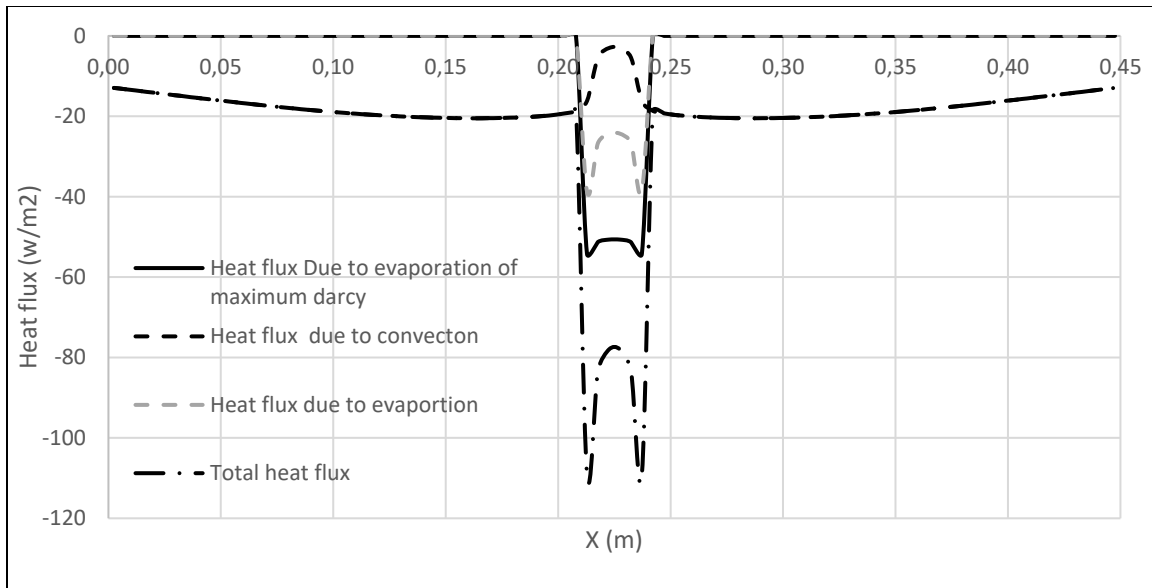


Figure 3.11 Heat flux components for  $T_{\text{air}} = 5 \text{ }^{\circ}\text{C}$  and  $T_{\text{water}} = 15 \text{ }^{\circ}\text{C}$

### 3.2.3 Convection coefficient

Figure 3.12 shows the effect of the coefficient of convection ( $h_c$ ) on the temperature of the surface on the concrete. It can be seen that the temperature on the surface increases with increase of the coefficient of convection. For the higher  $h_c$ , the evaporation rate causes a decrease on the temperature in the joint area comparing to the other parts. For the  $h_c = 1 \text{ W}/(\text{m}^2 \cdot \text{K})$ , there is an increase in temperature on the joint area. The reason is  $h_c$  is very low for water to gain heat for evaporation. But as water has higher conductivity compared to other parts, the moisture content in joint lead to small temperature increase in the joint.

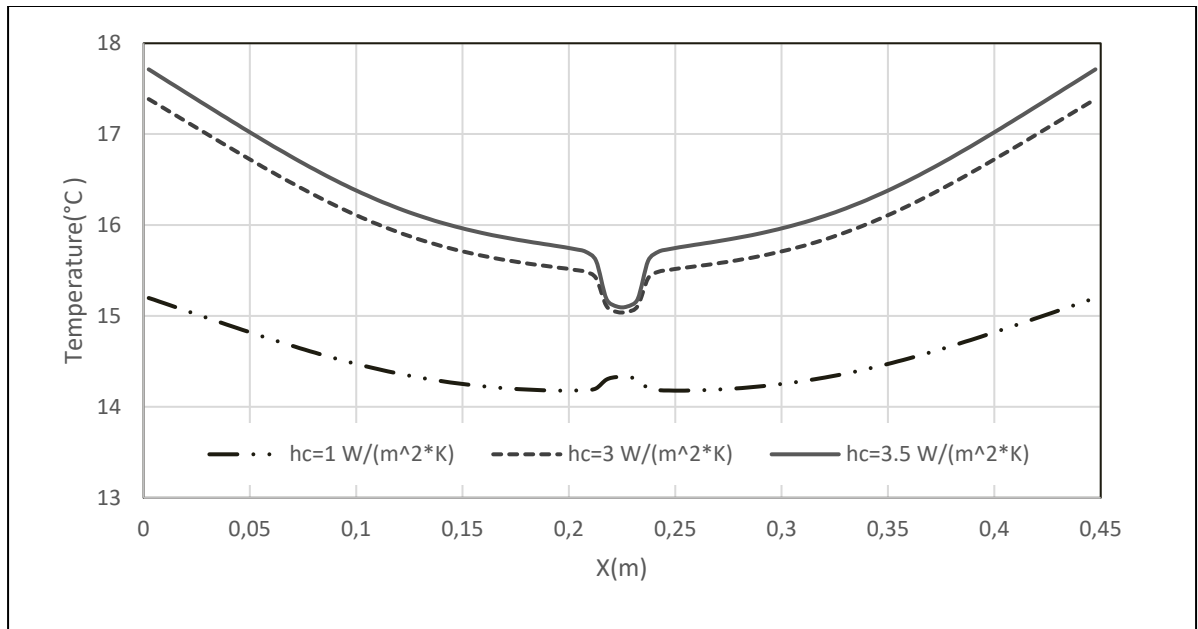


Figure 3.12 Influence of hydraulic conductivity on the temperature on the surface of concrete for  $T_{air}=20.5^{\circ}\text{C}$  and  $T_{water}=13^{\circ}\text{C}$

### 3.2.4 Joint permeability

Figure 3.13 shows the effect of joint permeability on the temperature of concrete surface. As you can see in these graphs which are in base condition,  $T_{air} = 20.5^{\circ}\text{C}$  and  $T_{water} = 13^{\circ}\text{C}$  and  $h_r = 0.56$ , temperatures on the surface decreases as the joint permeability increases. For the higher permeability the temperature has the lowest temperature. The reason might be related to the lower temperature of underground water as well as the evaporation effect on the joint.

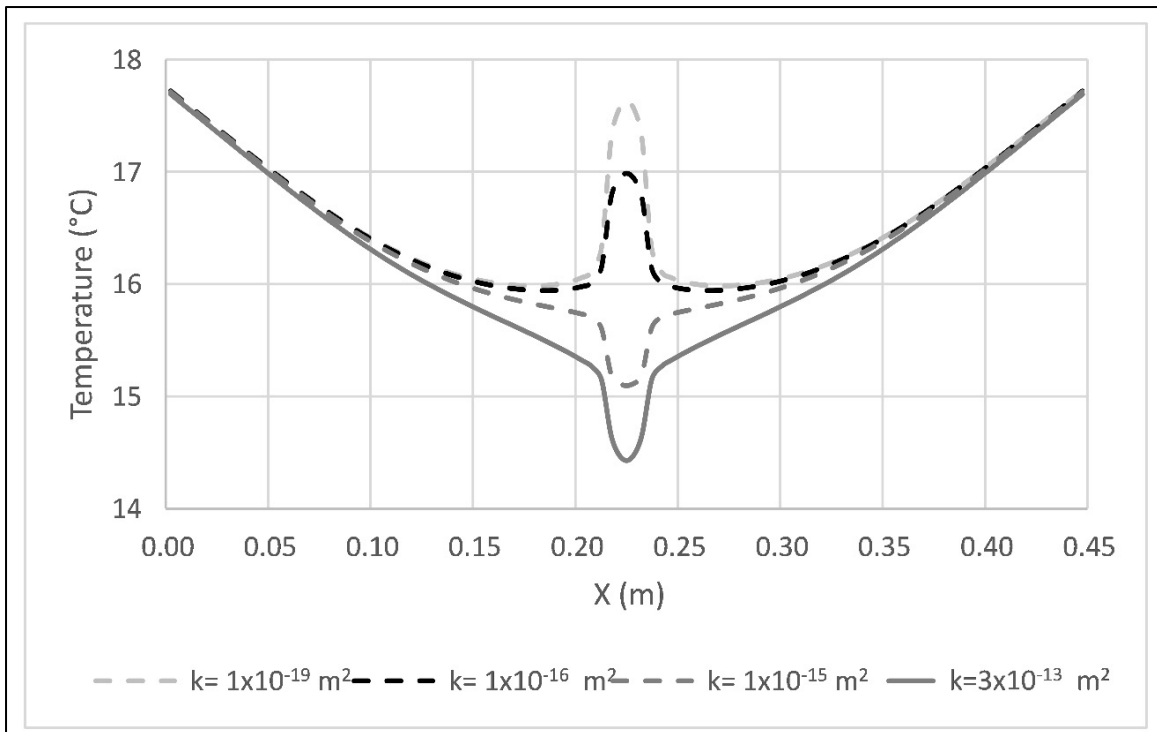


Figure 3.13 Influence of joint permeability on the temperature on the concrete surface for  $T_{air} = 20.5 \text{ }^\circ\text{C}$  and  $T_{water} = 13 \text{ }^\circ\text{C}$

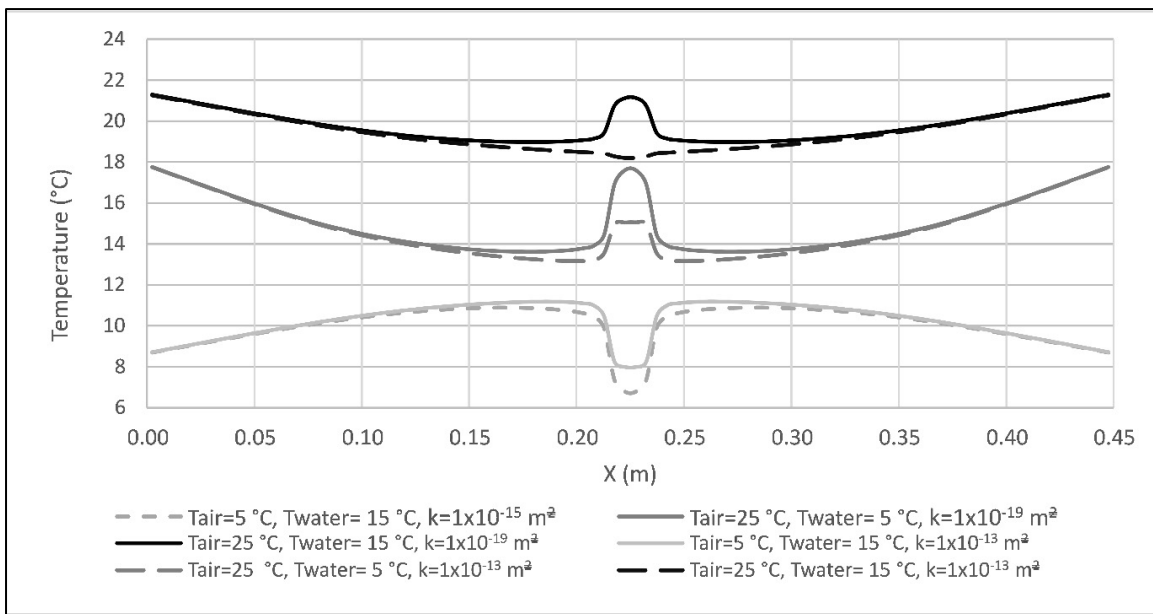


Figure 3.14 Comparison of temperature on the concrete surface for different water and air temperature and joints permeabilities

Figure 3.14 compares concrete temperatures for different water and air temperatures, as well as joints permeability. The two first graph from top, show the temperature on concrete for two permeabilities  $k = 1 \times 10^{-13} \text{ m}^2$  and  $k = 1 \times 10^{-19} \text{ m}^2$  for  $T_{\text{air}} = 25 \text{ }^\circ\text{C}$  and  $T_{\text{water}} = 15 \text{ }^\circ\text{C}$ . As it can be seen the temperature on the joints is lower for the higher permeability of  $k = 1 \times 10^{-13} \text{ m}^2$  as was expected due to evaporation and water temperature effect. The two graph in the middle show the temperature on concrete for the same permeabilities as above ( $k = 1 \times 10^{-13} \text{ m}^2$  and  $k = 1 \times 10^{-19} \text{ m}^2$ ) for  $T_{\text{air}} = 25 \text{ }^\circ\text{C}$  and  $T_{\text{water}} = 5 \text{ }^\circ\text{C}$ . For this case also the temperature on the joints is lower for the higher permeability of  $k = 1 \times 10^{-13} \text{ m}^2$  for the reason that was explained. The two last set graphs show the temperature for  $T_{\text{air}} = 5 \text{ }^\circ\text{C}$  and  $T_{\text{water}} = 15 \text{ }^\circ\text{C}$  for two permeabilities  $k = 1 \times 10^{-13} \text{ m}^2$  and  $k = 1 \times 10^{-15} \text{ m}^2$ . In this case according to graphs, the temperature on the joint shows higher temperature for higher permeability ( $k = 1 \times 10^{-13}$ ). In this scenario, the temperature of water is higher than air temperature and there is less evaporation due to lower temperature of air compared to water. There might be the reason why more permeabilities might lead to a higher temperature.

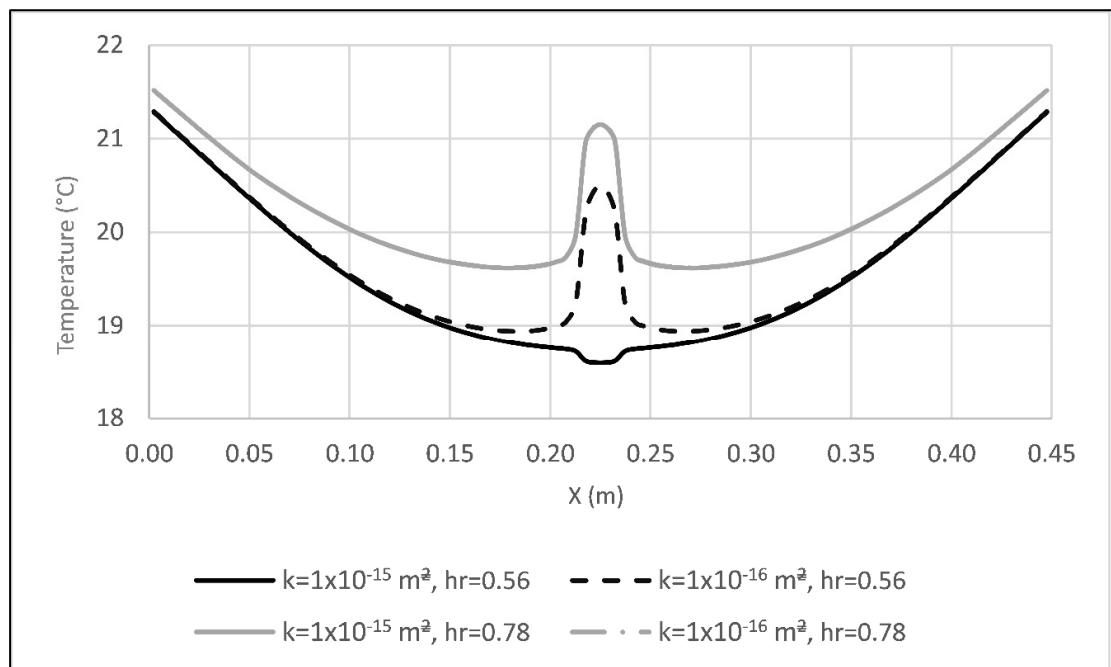


Figure 3.15 Influence of relative humidity and permeabilities on the temperature on the concrete surface for  $T_{\text{air}} = 25 \text{ }^\circ\text{C}$  and  $T_{\text{water}} = 15 \text{ }^\circ\text{C}$

As shown in Figure 3.15, an evaluation of the effect of relative humidity on the surface of concrete is presented for two permeabilities that are close to one another. Solid black line shows the temperature for  $k=1 \times 10^{-15} \text{ m}^2$  and the dash black line shows the temperature for  $k=1 \times 10^{-16} \text{ m}^2$  for relative humidity of 0.56. For two close permeabilities, as it can be seen, there is a noticeable difference in temperature at the joint surface. This shows the importance of influence of permeabilities on the temperature variance on the concrete for base relative humidity. For gray graph located at the top of the graphs, the temperature on concrete surfaces is plotted for the same permeabilities ( $k=1 \times 10^{-15} \text{ m}^2$   $k=1 \times 10^{-16} \text{ m}^2$ ) while the relative humidity is changed from 0.56 to 0.78. In fact, the gray graph is consisting of two graphs that were overlapped since they have the same temperature for two permeabilities. As evident from the graph, temperature variations resulting from small changes in permeability are difficult to detect for higher relative humidity levels. This shows the importance of relative humidity on the temperature variation along the concrete surface. As it can be seen the temperature difference due to the small variation of permeabilities can not be determined for higher relative humidity. The other interesting point which can be concluded from this graph is, for two different scenarios having similar value of permeability, water and air temperature, The joint experience higher temperature when the relative humidity is higher.

### 3.2.5 Temperature anomaly graphs

In this study, the temperature anomaly graphs defines the temperature difference between the center of the joint and a point located 10 cm away from the joint. The temperature anomaly can be plotted versus either the flow rate or the permeability. Because as mention in equation 1.4, flow rate and permeabilities are related according to Dracy's law. Figures 3.16 and 3.17 show schematic representations of the temperature measurement points on the model and on a temperature graph.

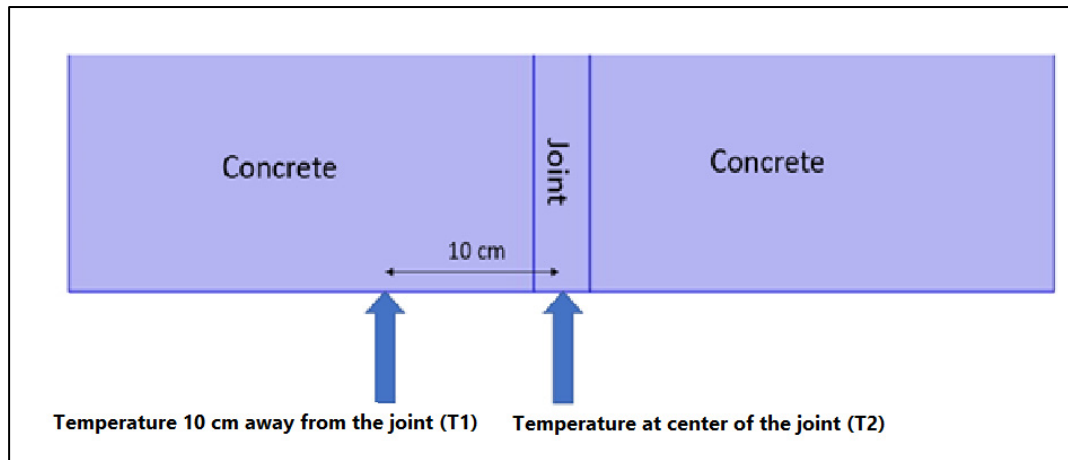


Figure 3.16 Location of temperature values for temperature anomaly graphs

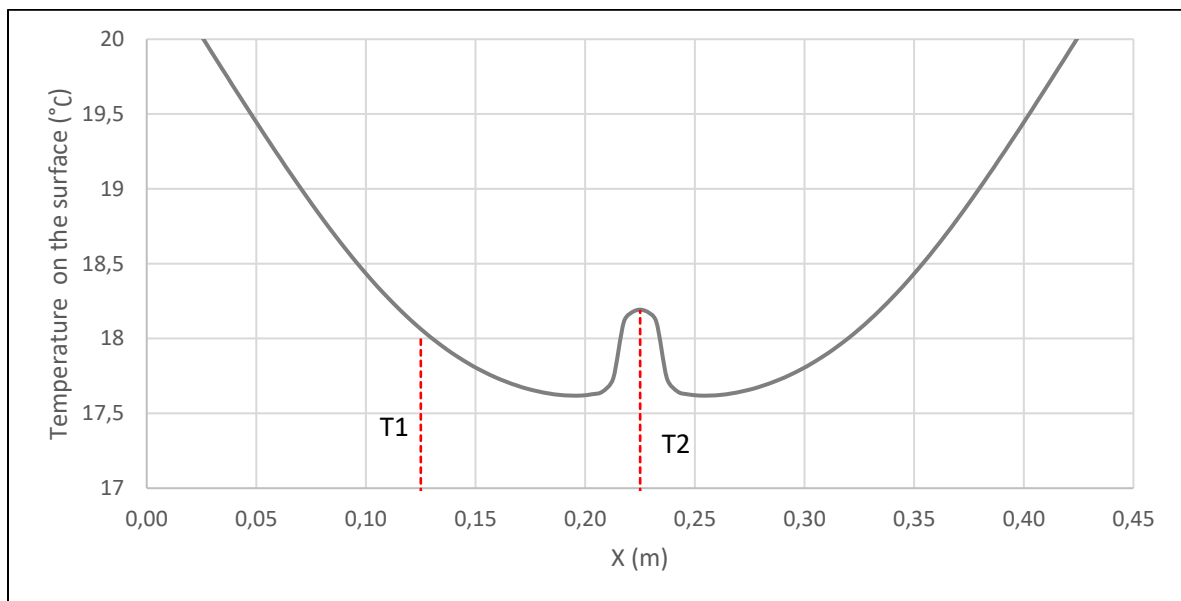


Figure 3.17 Points on the temperature curve for calculating the temperature anomaly

Figure 3.18 shows the relationship between the temperature anomaly and joint permeability for different value of relative humidity. For permeability values below  $1 \times 10^{-15} \text{ m}^2$ , the environmental conditions control the temperature anomaly. The air temperature, relative humidity and the convection coefficient control the evaporation rate and the heat transfer between air and joint. For permeability values between  $1 \times 10^{-15} \text{ m}^2$  and  $1 \times 10^{-13} \text{ m}^2$ , the temperature anomaly is controlled by both the groundwater temperature and environmental

condition. For a higher permeability or higher flow rate, the temperature anomaly is controlled by the groundwater temperature. For the lower flow rate or permeabilities, the evaporation is limited by Darcy flux (equation 2.2). For a higher permeability, it is equation 2.4 that controls the evaporation.

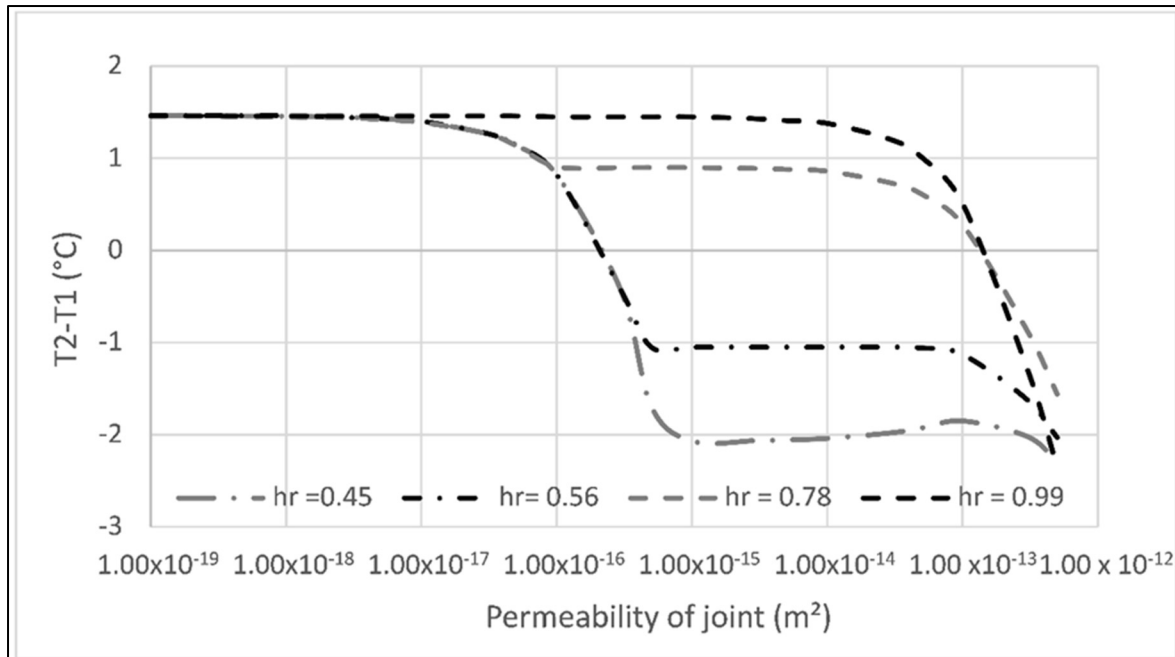


Figure 3.18 Influence of relative humidity on temperature anomalies graph for  $T_w=13$  (°C) and  $T_{air}=20.5$  (°C)

Figure 3.19 shows the influence of the  $h_c$  on the temperature anomaly. For  $h_c$  of  $1 \text{ W}/(\text{m}^2 \cdot \text{K})$  and for the permeability between  $1 \times 10^{-16} \text{ m}^2$  and  $1 \times 10^{-13} \text{ m}^2$ , it can be seen that the temperature anomaly is 0. The temperature anomaly will be increasingly negative with the increase of  $h_c$ . For the coefficient convection also like relative humidity parameters, it is for the lower flow rate that is influenced by this factor and evaporation, for higher flow rate, the anomaly is controlled by underground water temperature.

Figure 3.20 shows the temperature anomalies for different water and air temperature. As it is evident, more temperature differences between air and water temperature lead to more anomaly. As with the previous figures, for a lower permeability, the temperature anomaly is

controlled by environmental conditions, for the middle part of graphs, the temperature control by both evaporation and groundwater temperature and for higher permeability the anomaly control by underground water temperature.

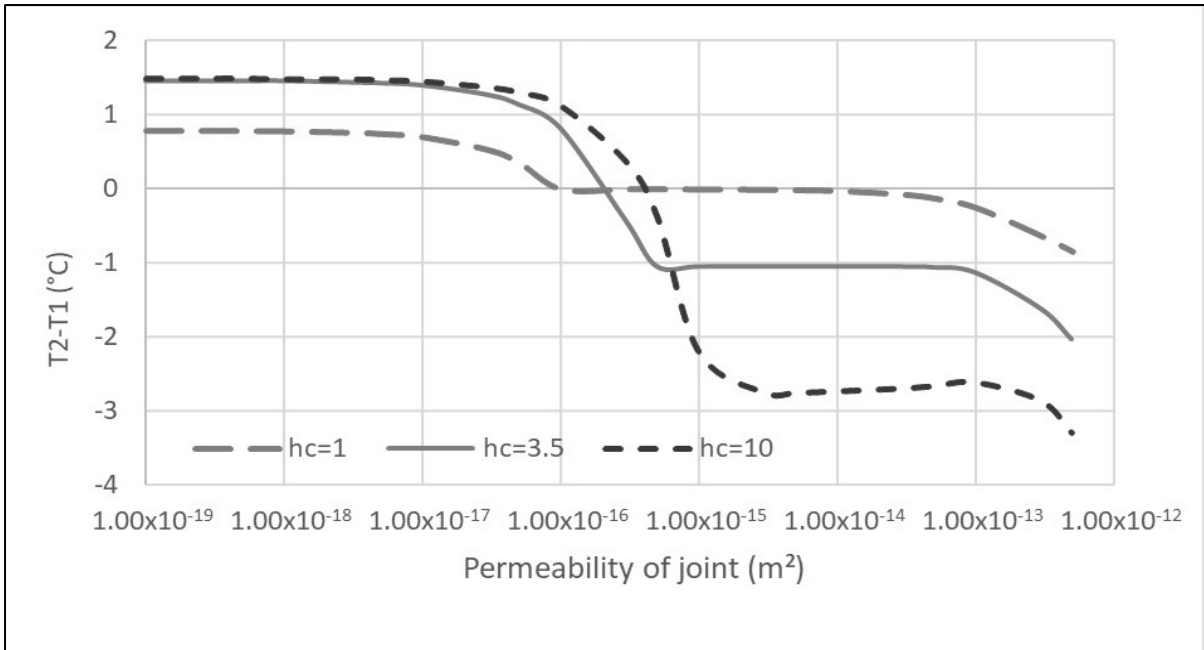


Figure 3.19 Influence of coefficient of convection on temperature anomalies graph for  $T_w=13$  (°C) and  $T_{air}=20.5$  (°C)

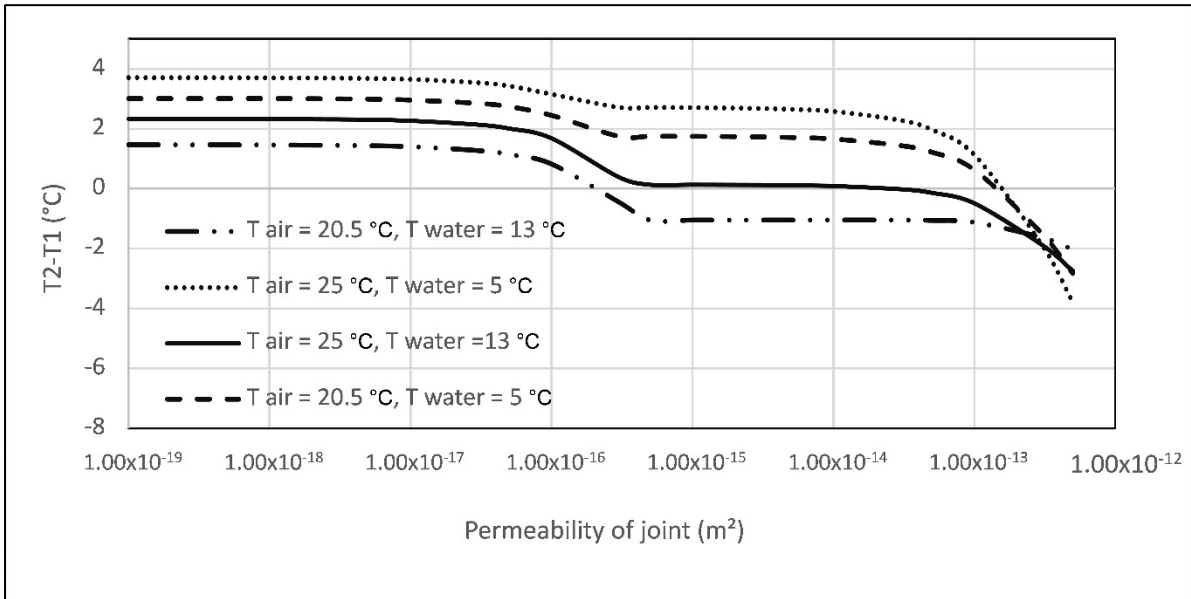


Figure 3.20 Influence of water and air temperature variation on temperature anomalies graph

## CONCLUSION

A parametric sweep allows to investigate the influence of each parameter on the temperature of wall surface inside the tunnel.

The temperature anomaly varies with the difference between the water and air temperatures. For permeability between  $1 \times 10^{-17} \text{ m}^2$  and  $1 \times 10^{-15} \text{ m}^2$ , the temperature anomaly is controlled by the environmental condition. Environmental conditions include air temperature, relative humidity and the convection coefficient. These parameters control the evaporation rate and the heat transfer between the air, the joint and the concrete surface. For higher permeability values, the anomaly is controlled by the groundwater temperature.

The following points can be extracted from temperature anomaly graphs:

- Temperature anomalies are more positive when there is a greater temperature difference between water and air.
- The temperature anomaly is positive for higher relative humidity values and negative for lower relative humidity values (considering the others parameters were assumed constant).
- A negative temperature anomaly increases with an increase in the coefficient of convection.

The temperatures profiles or the temperature variation along the surface results show:

- The temperature variation along the concrete surface is not constant for a temperature difference of 0 between water and air temperature (for example water and air temperature of  $13 \text{ }^\circ\text{C}$ ). In contrary, for water temperature  $11.5 \text{ }^\circ\text{C}$  and air temperature  $20.5 \text{ }^\circ\text{C}$  and also for an air temperature of  $22.75 \text{ }^\circ\text{C}$  and a water temperature of  $13 \text{ }^\circ\text{C}$ , the temperature remains relatively constant along the concrete and joint surface. (the other parameters were assumed in base condition).
- For higher relative humidity, it is difficult to detect the temperature variation associated to close permeabilities.
- More difference between water and air temperature lead to more temperature variation on the concrete surface.

- The increase in permeability causes the joint surface to experience a higher temperature drop.
- The increase in relative humidity led to temperature increase on the joint, in comparison with lower relative humidity scenarios.
- A high relative humidity will result in a diminished rate of water evaporation and a decrease in heat transfer.
- For higher relative humidity the temperature difference between concrete and joint decrease.

The parametric studies show the following results about heat flux on the model:

- The total heat flux varies according to water and air temperature variation.
- On the joint, the total heat flux is 0 for water and air temperature of 13°C and 20.5 °C (base condition). In this situation the evaporation on the joint considered to be limiting factor while on concrete convection components considered to be controlling factor.
- The total heat flux is positive for water and air temperature of 5 °C and 25 °C.
- Finally for an opposite scenario when water is 15 °C and air is 5 °C, the total heat flux on the joint is negative.

Water infiltration characterization for tunnel joints using thermography is a challenging task. To develop an accurate numerical model, precise input data must be collected. Moreover, there are many environmental factors that influence the thermal image quality and results.

## RECOMMENDATIONS

There are some recommendations to improve the results accuracy for next studies, those are including:

- There is no study regarding the influence of the shape of joints (for example, circular shapes) on temperature anomalies and this can be done by developing a new physical and numerical modeling.
- It is necessary to develop more complex models to take into the consideration the influence of freezing and melting on the leakage flow rates and on the temperature pattern on the concrete surface.
- Temperature variation has a influence on the permeability of joints and cause change in permeabilities, this effect must be taken into accounts for future studies.
- The corners of the model were some sources of errors, for the next studies, this effect should be removed.
- Having a geotechnical and hydrogeology study performed in the real tunnel would be an excellent opportunity to gather real data for usage in both numerical and experimental model. For example, collecting the permeabilities pattern, flow rate information and also recording thermal image of infiltration site are considered valuable information to use in both numerical and experimental mode



## REFERENCES

- Avdelidis, N. P., & Moropoulou, A. (2004). Applications of infrared thermography for the investigation of historic structures. *Journal of Cultural Heritage*, 5(1), 119-127.
- Branco, F., Tadeu, A., & Simoes, N. (2004). Heat conduction across double brick walls via BEM. *Building and Environment*, 39(1), 51-58.
- Barreira, E., Almeida, R. M., & Moreira, M. (2017). An infrared thermography passive approach to assess the effect of leakage points in buildings. *Energy and Buildings*, 140, 224-235.
- Bejan, A. (2013). *Convection heat transfer* (4<sup>th</sup> ed.). John Wiley & Sons.
- Comsol Multiphysics. (2019). *Heat Transfer Module User's Guide V5.5* (Part number: CM020801). Burlington, MA: COMSOL, Inc, [www.comsol.com](http://www.comsol.com)
- CETU, Centre d'Études des Tunnels. (2015). *Road tunnel civil engineering inspection guide, Book 1: from disorder to analysis, from analysis to rating*. France. Retrieved from <http://www.cetu.developpement-durable.gouv.fr/IMG/pdf>
- Dong, W., Chen, Y., Bao, Y., & Fang, A. (2020). A validation of dynamic hygrothermal model with coupled heat and moisture transfer in porous building materials and envelopes. *Journal of Building Engineering*, 32, 101484. <https://doi.org/10.1016/j.jobe.2020.101484>
- Domenico, P. A., & Schwartz, F. W. (1998). *Physical and Chemical Hydrogeology* (2<sup>th</sup> ed.). New York: John Wiley & Sons.
- Duhaime, F., Pirnia, P., Klotoé, C., St-Laurent, X., M'Nasri, S., & Chapuis, R. P. (2019). *Infiltrations d'eau dans le tunnel Ville-Marie : caractérisation et pistes de solutions* (Projet R793.1 – Phase 3). Montréal: École de technologie supérieure.
- Flir. (2012). *The Ultimate Infrared Handbook for R&D Professionals*, Flir, Boston, Ma.
- Font Capó, J. (2012). *Interaction between groundwater and TBM (Tunnel Boring Machine) excavated tunnels*. (Doctoral thesis, UPC, Departament d'Enginyeria del Terreny, Spain). Retrieved from <http://hdl.handle.net/2117/94692>
- Gong, C., Ding, W., Soga, K., Mosalam, K. M., & Tuo, Y. (2018). Sealant behavior of gasketed segmental joints in shield tunnels: An experimental and numerical study. *Tunnelling and Underground Space Technology*, 77, 127-141. <https://doi.org/10.1016/j.tust.2018.03.029>

- Hare, D. K., Briggs, M. A., Rosenberry, D. O., Boutt, D. F., & Lane, J. W. (2015). A comparison of thermal infrared to fiber-optic distributed temperature sensing for evaluation of groundwater discharge to surface water. *Journal of Hydrology*, 530, 153-166.
- Haack, A., Schreyer, J., & Jackel, G. (1995). Report to ITA Working Group on Maintenance and Repair of underground structures: State-of-the-art of non-destructive testing methods for determining the state of a tunnel lining. *Tunnelling and Underground Space Technology Incorporating Trenchless*, 10(4),413-431.
- Jerman, M., & Černý, R. (2012). Effect of moisture content on heat and moisture transport and storage properties of thermal insulation materials. *Energy and Buildings*, 53, 39-46.
- Ji, Z., Lu, K. C., & Ma, C. C. (2012). Classification causes of tunnel frost damages in cold region and several new technologies to prevent them. In *Applied Mechanics and Materials* (Vol. 170, pp. 1504-1510). Trans Tech Publications Ltd.
- Kong, F., & Zhang, Q. (2013). Effect of heat and mass coupled transfer combined with freezing process on building exterior envelope. *Energy and Buildings*, 62, 486-495. <https://doi.org/10.1016/j.enbuild.2013.03.012>
- Klotoé, C. H., Duhaime, F., & Guizani, L. (2018). *Thermal and hydraulic modelling of road tunnel joints*. Paper presented at Conference COMSOL 2018, Boston.
- Kylili, A., Fokaides, P. A., Christou, P., & Kalogirou, S. A. (2014). Infrared thermography (IRT) applications for building diagnostics: A review. *Applied Energy*, 134, 531-549.
- Kosmatka, S. H., Kerkhoff, B., Panarese, W., MacLeod, N., & McGrath, R. (2011). *Design and control of concrete mixtures* (8<sup>th</sup> ed.). Association Canadian Cement Company, Ottawa, Ontario, Canada
- Lerma, J. L., Cabrelles, M., & Portalés, C. (2011). Multitemporal thermal analysis to detect moisture on a building façade. *Construction and Building Materials*, 25(5), 2190-2197. <https://doi.org/10.1016/j.conbuildmat.2010.10.007>
- Li, F., Li, Q., Meng, Q., Liu, J., Mao, H., Xie, J., & Liu, J. (2021). Effect of moisture on the thermal performance of exterior walls in the tropical islands of the South China Sea. *Applied Thermal Engineering*, 186, 116505. <https://doi.org/10.1016/j.applthermaleng.2020.116505>
- Liu, X., Chen, Y., Ge, H., Fazio, P., & Chen, G. (2015). Numerical investigation for thermal performance of exterior walls of residential buildings with moisture transfer in hot summer and cold winter zone of China. *Energy and Buildings*, 93, 259-268. <https://doi.org/10.1016/j.enbuild.2015.02.016>

- Liu, Y., Wang, Y., Wang, D., & Liu, J. (2013). Effect of moisture transfer on internal surface temperature. *Energy and buildings*, 60, 83-91.
- Locatelli, L., Di Marco, G., Zanichelli, C., & Jarre, P. (2001, June). *Rehabilitation of highway tunnels: Techniques and procedures*. Paper presented at World Tunnel Congress, Milan, Italy.
- Lu, Z., Zhu, F., Shi, L., Wang, F., Zeng, P., Hu, J., ... & Chen, Q. (2019). Automatic seepage detection in cable tunnels using infrared thermography. *Measurement Science and Technology*, 30(11), 115902.
- Meola, C., & Carlomagno, G. M. (2004). Recent advances in the use of infrared thermography. *Measurement science and technology*, 15(9), R27.
- Maldague, X. P. (1993). Overview of nondestructive evaluation (NDE) using infrared thermography. In *Nondestructive evaluation of materials by infrared thermography* (pp. 1-22). Springer, London. <https://doi.org/10.1007/978-1-4471-1995-1>
- Mainali, G., Dineva, S., & Nordlund, E. (2015). Experimental study on debonding of shotcrete with acoustic emission during freezing and thawing cycle. *Cold Regions Science and Technology*, 111, 1–12. <https://doi.org/10.1016/j.coldregions.2014.11.014>
- M'nasri, S. (2020). *Construction d'un modèle physique de joints de dilatation pour l'étude de la relation entre la température du béton et la perméabilité des joints* (maîtrise dissertation, École de technologie supérieure, Montreal, QC).
- Morin-Morissette, P.O. (2016). *Étude de la durabilité à l'écaillage en présence de sel fondant des bétons avec liant ternaire*. (Mémoire de maîtrise, Université de Sherbrooke, Sherbrooke, QC). Retrieved from <https://savoirs.usherbrooke.ca/handle/11143/10503>.
- Mundy, E., Gleeson, T., Roberts, M., Baraer, M., & McKenzie, J. M. (2017). Thermal imagery of groundwater seeps: Possibilities and limitations. *Groundwater*, 55(2), 160-170.
- Mainali, G., Dineva, S., & Nordlund, E. (2015). Experimental study on debonding of shotcrete with acoustic emission during freezing and thawing cycle. *Cold Regions Science and Technology*, 111, 1-12. <https://doi.org/10.1016/j.coldregions.2014.11.014>
- Nawy, E. (2008). Joints in Concrete Construction. In E. Nawy (Ed.), *Concrete Construction Engineering Handbook*. Boca Raton: CRC Press. <https://doi.org/10.1201/9781420007657>
- Nield, D. A., & Bejan, A. (2012). *Convection in porous media* (4<sup>th</sup> ed.). New York: springer <https://doi.org/10.1007/978-1-4614-5541-7>

- Nilsson, L. O. (2004). Moisture Transport in cementitious materials—Theory and some experimental results. In Jensen, O. M., Geiker, M., & Stang, H. (Eds), *Knud Højgaard Conference on Advanced Cement-Based Materials: Research and Teaching* (1st ed, pp.187-205). Technical University of Denmark, Lyngby, Denmark: BYG-DTU
- Peltier, M., Loria, A. F. R., Lepage, L., Garin, E., & Laloui, L. (2019). Numerical investigation of the convection heat transfer driven by airflows in underground tunnels. *Applied Thermal Engineering*, *159*, 113844.
- Pappalardo, G. (2018). First results of infrared thermography applied to the evaluation of hydraulic conductivity in rock masses. *Hydrogeology Journal*, *26*(2), 417-428.
- Philip, J. R., & De Vries, D. A. (1957). Moisture movement in porous materials under temperature gradients. *Transactions American Geophysical Union*, *38*(2), 222-232. <https://doi.org/10.1029/TR038i002p00222>
- Solecki, A., Eng, P., Waher, K., Eng, P., Kramer, G., & Eng, P. (2022). TBM Tunnelling Challenges and Managing High Groundwater Inflows on the Ashbridges Bay Treatment Plant Outfall Project. *Tunneling for the Future – Sustainable and Smart*.
- Shijie, Z., Guyi, Z., Deming, L., Shuyi, W., Fei, S., & Chao, W. (2020). The crucial techniques of water leakage treatment in operating highway tunnel. *IOP Conference Series: Earth and Environmental Science*, *525*(1), 012160. <https://doi.org/10.1088/1755-1315/525/1/012160>
- Tseng, D. J., Tsai, B. R., & Chang, L. C. (2001). A case study on ground treatment for a rock tunnel with high groundwater ingress in Taiwan. *Tunnelling and Underground Space Technology*, *16*(3), 175-183.
- Toshihiro, A., & Yoshiyuki, K. (2003). Tunnel maintenance in Japan. *Tunnelling and Underground Space Technology*, *18*(2/3), 161-169.
- Tariku, F., Kumaran, K., & Fazio, P. (2010). Transient model for coupled heat, air and moisture transfer through multilayered porous media. *International Journal of Heat and Mass Transfer*, *53* (15–16), 3035–3044. <https://doi.org/10.1016/j.ijheatmasstransfer.2010.03.024>
- Vollmer, M., & Möllmann, K. P. (2010). *Fundamentals of infrared thermal imaging* (1st ed.). Weinheim: Wiley-VCH.
- Wang, X., Jin, X., Yin, Y., Wang, X., Shi, X., & Zhou, X. (2020). Study on non-isothermal moisture transfer characteristics of hygroscopic building materials: From parameter characterization to model analysis. *Energy*, *212*, 118788. <https://doi.org/10.1016/j.energy.2020.118788>

- Wang, X., Jin, X., Yin, Y., Shi, X., & Zhou, X. (2021). A transient heat and moisture transfer model for building materials based on phase change criterion under isothermal and non-isothermal conditions. *Energy*, 224, 120112.
- Wang, Y., Ma, C., Liu, Y., Wang, D., & Liu, J. (2018). Effect of moisture migration and phase change on effective thermal conductivity of porous building materials. *International journal of heat and mass transfer*, 125, 330-342.
- Wimsatt, A., White, J., Leung, C., Scullion, T., Hurlebaus, S., Zollinger, D., ... National Academies of Sciences, Engineering, and Medicine (2013). Mapping Voids, Debonding, Delaminations, Moisture, and Other Defects Behind or Within Tunnel Linings. *Transportation Research Board*. <https://doi.org/10.17226/22609>
- Yuan, C., Li, S., & Li, S. (2011). Study on the defects characteristics of water leaking of old tunnels in cold regions. In *Tunnel management, emerging technologies, and innovation* (pp. 187-193). [https://doi.org/10.1061/47632\(411\)24](https://doi.org/10.1061/47632(411)24)
- Williams, M. E. (2014). Repair of deteriorated bridge substructures using carbon fiber-reinforced polymer (CFRP) composites. In *Advanced Composites in Bridge Construction and Repair* (pp. 265-286). Woodhead Publishing.